energies

MDPI

Article

Experimental Study on the Optimal-Based Vibration Control of a Wind Turbine Tower Using a Small-Scale Electric Drive with MR Damper Support

Paweł Martynowicz

Department of Process Control, AGH University of Science and Technology, Mickiewicza 30 Ave., 30-059 Kraków, Poland; pmartyn@agh.edu.pl

Abstract: The paper presents an experimental implementation of an optimal-based vibration control for a scaled wind turbine tower-nacelle structure. A laboratory model of the approximate power scale of 340 W, equipped with a nonlinear tuned vibration absorber (TVA), is analysed. For control purposes, a combined operation of a small-scale electric servo drive and a magnetorheological (MR) damper is used in the TVA system. Nonlinearities of both the electric drive and the MR damper are intrinsic parts of the adopted nonlinear control concept. The aim of the research is the simple-hardware real-time implementation and the experimental investigation of the simultaneous actuator and damper control, including the analysis of the influence of optimal control law parameters and quality function weights on the vibration attenuation efficiency and actuator energy demand. As a reference, an optimal-based, modified ground-hook control with the single goal of the primary structure deflection minimisation is used along with the passive system with zero MR damper current and idling electric actuator, proving the advantages of the proposed method. The regarded solutions guarantee 57% maximum structure deflection reduction concerning the passive TVA configuration, using an MR damper of 32 N maximum force and an electric drive of 12.5 N nominal force and 0.76 W nominal power. An interesting alternative is the optimal control concept tuned with regard to the actuator power minimisation—it provides 30% maximum structure deflection attenuation (concerning the passive TVA configuration) while using a passive damper of 3.3 N maximum force and an actuator of 0.17 W nominal power only. It makes evident the advantage of the properly tuned optimal control algorithm over the modified ground-hook law—it requires 51% less actuator energy than the latter parametrised to exhibit the same vibration attenuation properties.

Keywords: real-time vibration control; optimal-based control; wind turbine; hybrid tuned vibration absorber; electric drive; magnetorheological damper

Citation: Martynowicz, P. Experimental Study on the Optimal-Based Vibration Control of a Wind Turbine Tower Using a Small-Scale Electric Drive with MR Damper Support. *Energies* **2022**, *15*, 9530. https://doi.org/10.3390/en15249530

Academic Editor: Mohamed Benbouzid

Received: 15 October 2022
Accepted: 12 December 2022
Published: 15 December 2022

1. Introduction

Mechanical vibrations are problematical phenomena concerning slender structures such as towers, masts, chimneys, bridges [1,2], skyscrapers [3–5], wind turbines [6–10], as well as plate structures [11,12], etc. Most of them are fitted with dedicated solutions for vibration minimisation and fatigue reduction, such as tuned vibration absorbers/tuned mass dampers (TVAs/TMDs), tuned liquid column dampers (TLCDs), bracing systems, etc. [13–18]. TVAs are more and more widely spread vibration reduction systems. A standard (passive) TVA is built as an additional mass connected with the protected structure by a spring and a viscous damper (in parallel), the parameters of which are tuned to the selected mode of the vibration [19]. Passive TVAs cope reasonably well with the vibration of a single frequency but cannot adapt to a broader spectrum [8]. During the structure exploitation lifespan, its frequency response may vary due to i.a. temperature fluctuations, icing, or external loading, apart from the defects that may arise. Thus, more advanced TVA systems have been investigated. Hybrid TVAs (H-TVAs), being the parallel connection

of a passive TVA with active actuators [5], are the most dependable systems used in civil engineering [15,20–23]. The active force of the H-TVA increases the vibration attenuation efficiency and robustness of the TVA, while its energy, power, and force requirements are much lower than those of an active TVA (i.e., a TVA in which an active actuator replaces a viscous damper) of comparable performance. The devices used for the structural vibration control include active electro-hydraulic/-pneumatic/-magnetic actuators, semi-active magnetorheological (MR) or changeable-orifice dampers, or passive devices such as viscoelastic/hydraulic/friction/granular dampers, etc. [13–15,24].

Most of the (active or semi-active) actuator real-time control solutions are based on the bang-bang strategy [25], fuzzy logic, or two-stage algorithms that consist of the determination of an actuator's required force and its accurate tracking [2,26,27]. The latter concepts experience an inability to produce the required (by the first stage algorithm) force pattern due to the actuator nonlinearities/constraints (including the ever-present force and stroke constraints), the impossibility of generating active forces for semi-active actuators, etc. The stroke limitation of the real-world vibration reduction system, specifically the TVA, is frequently addressed by the use of end-stop bumpers or spring-damper buffer systems [28], which prevent the collision with the primary structure but compromise the control quality at the same time (the presence of the additional springs also alters the TVA tuning frequency within the buffer ranges). As a result, the force pattern determined to be optimal (at the first stage) is not the same as the actuator's output. Some sophisticated algorithms require real-time frequency determination, which may be problematic for polyperiodic or random vibrations.

The idea of a concurrent, parallel operation of the MR damper and the active actuator has only occasionally been investigated, to mention just a few references. Kim et al. [29] used a parallel, concentric connection of the three actuators: a passive air spring, an MR damper, and an electromagnetic coil actuator in a precision machine mount to isolate it from unwanted vibrations. The pneumatic forces constantly supported the heavy weight of an upper structure, the MR damper handled the transient response, while the electromagnetic actuator reduced the resonance response, which was switched mutually with regard to the velocity threshold (the control signal was applied either to the MR damper or the active device). Switching logic was implemented to resolve the problem of interference between the MR damper and active actuator control forces. A simple proportional controller was applied to the MR damper, while a proportional-derivative circuit was applied to the electromagnetic and pneumatic devices. Sophisticated hardware was required to treat the high sampling rate. The parallel combination of the MR damper and active air spring in a hybrid mount system designed for vibration isolation was investigated in [30]. The air spring was used to support the precision stage and to isolate the large loads by controlling the spring coefficient. Additionally, the MR damper force was produced to control the extensive vibrations. The isolation performance was investigated by the utilisation of the simple PID controller for the air servo valve and the MR damper current. The vibration was reduced at low frequencies, yet the response amplitude at frequencies above 30 Hz was slightly increased. In turn, the simultaneous operation of the MR damper arranged in series with the hydraulic cylinder in a bracing system of a shear frame model representing a monopile wind turbine structure was investigated in [31], adopting the linear control theory for the linearised system and actuator—the MR damper was used to emulate the behaviour of the idealised linear dash-pot. The hydraulic cylinder provided the correct displacement across the MR damper, while the bang-bang force tracking algorithm determined the MR damper control current. The controller activated high-frequency modes and generated drift in the actuator displacement, though. Thus, only a fraction of the measured damper force could be used as input to the designed integral force feedback in the real-time hybrid simulations.

With regard to the above considerations, the current study concerns a complex, hybrid MR TVA system (H-MR-TVA) utilising a parallel, concurrent operation of a small-scale electric servo drive [13,22,28,32–34] and an MR damper [2,4,35–41]. An MR damper exhibits

a wide range of resistance forces compared with a viscous damper, as well as a millisecond response time and only signal-level energy requirements, although it cannot add energy to the system when necessary (being a semi-active device); it also suffers from a nonzero remanent force [27,41–45]. On the other hand, a small-scale electric actuator may be used to generate the active forces and cancel the MR damper remanent force while using a modest amount of energy. Simulations and experiments have shown that implementing both an MR damper and a small electric drive in the TVA system may lead to state-of-the-art vibration reduction efficiency. The experimental implementation of a parallel operation of the simultaneously controlled MR damper and electric drive in the TVA system may be considered the originality of this work.

To cope with the control limitations (discussed above), the author devised a concept [34,40,41] to embed the nonlinearities of the actuators (i.e., the MR damper and the electric servo in the current study), including their force constraints, into a control problem formulation, removing efficiency and robustness issues that arise when a determined optimal-based control is imprecisely mapped or beyond the permissible actuator range. This requires the use of nonlinear control methods, which include maximum-principle-based methods [9,12,46], Lyapunov function-based methods [1,3,32,39,44], linearisation methods with linear optimal control theory (LQR/LQG/$H2/H\infty$) [3,13,28,33,37,47,48], etc. Each method group has advantages and disadvantages, including the high computational load necessary for real-time operation and control authority degradation due to disturbances or unmodelled dynamics. The deployment of a nonlinear maximum-principle-based control method that incorporates actuators' nonlinearities while providing relatively simple real-time hardware implementation is the major contribution of this study.

The concept of the maximum-principle-based nonlinear optimal (or optimal-based) control was previously investigated by the author [40], considering, in particular, a scaled wind turbine tower-nacelle model [41,49–54]. Wind turbines experience varying external loads, such as wind variations, wind shear, Karman vortices, blade passing, changeable inflow conditions for the blades, sea waves, and ice load, etc. Additionally, internal factors, such as rotating machinery unbalance, contribute to the structural vibration and fatigue wear of towers and blades. In order to investigate the problem of wind turbine tower vibrations, a scaled tower-nacelle laboratory model that exhibits partial dynamic similarity (i.e., similarity of motions of tower tips) with a real-world 1.5 MW Vensys82 structure was developed and built. It was assumed that a nacelle, a hub, a shaft, a generator, blades, and a gearbox would all be represented by the rigid body fixed to the top of the rod, modelling a tower. A horizontal force produced by a modal shaker may be applied to the rod modelling a tower or to the rigid body, representing a nacelle assembly. The laboratory model enabled the analysis of two initial bending modes of the tower-nacelle system; however, only the first mode was investigated in the current study, and H-MR-TVA was tuned to its frequency. Current research results may be transferred to a real-world wind turbine thanks to previously determined time, length, and force scale factors [53,54]. The approximate power scale of the laboratory model was 340 W.

The paper is organised as follows. In the next section, a regarded system is described. Subsequently, the optimal vibration control problem is formulated and solved, covering simultaneous MR damper and actuator control. Then, the implementation procedure, the experimental setup, and the test conditions are discussed. This is followed by the key section covering real-time control results. The paper is summarised with several conclusions.

2. A Regarded System

A scaled wind turbine tower-nacelle model is regarded as a protected structure whose first bending mode modal parameters are: mass m_1, stiffness k_1, and damping c_1. An H-MR-TVA of absorber mass m_2 and spring stiffness k_2 is considered (Figure 1). The movement of both m_1 and m_2 was constrained to be linear displacement x_1 and x_2 (accordingly) along the common axis (horizontal in Figure 1) of an applied excitation force F_e, modelling the resultant load applied to the nacelle. An MR damper and a force actuator (F_a) were both

built parallel to the spring. Although the force actuator was carefully selected to exhibit the lowest motion damping for the required output nominal force F_{nom}, its influence (excess damping) on the TVA operation was significant; thus, mass m_2 was increased with regard to the previous research [41] to 14.1% of the mass m_1 to obtain two local maxima of the primary system displacement (x_1) frequency response (see Section 7) [19], while stiffness k_2 was tuned accordingly. Both the MR damper and force actuator were used for control purposes. The values of the adopted system parameters are presented in Table 1.

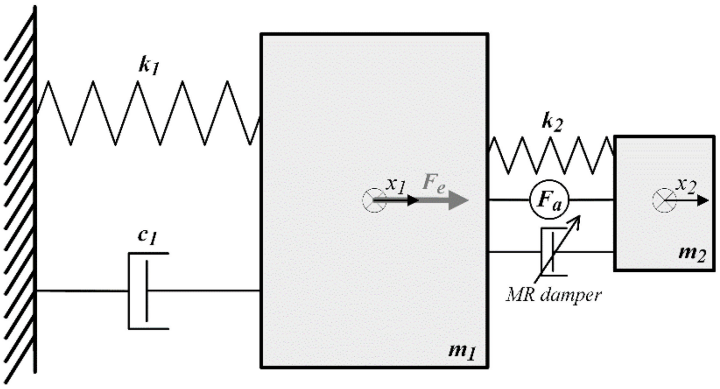

Figure 1. Two-body diagram of a regarded system with an H-MR-TVA.

Table 1. The adopted system parameters.

Parameter	Value
m_1	170.34 kg
k_1	82,554 N/m
c_1	49.53 Ns/m
m_2	24.01 kg (14.1% m_1)
k_2	8000 N/m
F_{nom}	12.5 N/6.25 N

Figure 2 presents the diagram of the theoretical passive TVA efficiency (vs. mass ratio, i.e., m_2/m_1), according to the authors of [19], represented by maximum nacelle displacement amplitudes $A(x_1)$ for the regarded primary structure parameters (Table 1); $A(\bullet)$ states for the amplitude. Two dots indicate mass ratios assumed in the current (14.1%) vs. previous research (7.7%) [41]. As it is commonly known, the TVA efficiency characteristic is nonlinear. The reduction in $A(x_1)$ due to the mass ratio increase to 14.1% was expected to be 23% only (concerning TVA of 7.7% mass ratio). However, a larger mass ratio contributes to lower TVA sensitivity to detuning [55].

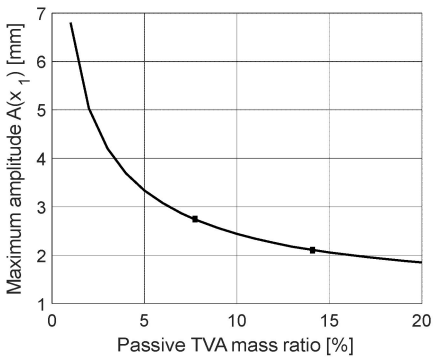

Figure 2. Maximum nacelle horizontal displacement amplitude $A(x_1)$ vs. passive TVA mass ratio (tuned according to [19]).

3. Control Problem Formulation and Solution

Consider the equation of motion of a vibrating structure with an H-MR-TVA:

$$\dot{z}(t) = f(z(t), u(t), t),\ t \in [t_0, t_1] \tag{1}$$

where $z(t)$ is a state vector:

$$z(t) = [z_1(t)\ \ z_2(t)\ \ z_3(t)\ \ z_4(t)]^T, \tag{2}$$

$u(t) = \begin{bmatrix} u_1(t) & u_2(t) \end{bmatrix}^T \in U\ (U = R^2)$ is a piecewise-continuous control vector, and a quality index to be minimised is:

$$G(z, u) = \int_{t_0}^{t_1} g(z(t), u(t), t)dt. \tag{3}$$

Following Section 2, assume: $z_1 = x_1$, $z_2 = \dot{x}_1$, $z_3 = x_2$, $z_4 = \dot{x}_2$, thus:

$$f(z(t), u(t), t) = \begin{bmatrix} z_2(t) \\ \frac{1}{m_1}(-(k_1 + k_2)z_1(t) - c_1 z_2(t) + k_2 z_3(t) + F_{mr}(z(t), u(t), t) + F_a(u(t)) + F_e(t)) \\ z_4(t) \\ \frac{1}{m_2}(k_2 z_1(t) - k_2 z_3(t) - F_{mr}(z(t), u(t), t) - F_a(u(t))) \end{bmatrix} \tag{4}$$

where:

$$\begin{aligned} F_{mr}(z(t), u(t), t) = (C_1 i_{mr}(u(t), t) + C_2)\tanh\{\nu[(z_4(t) - z_2(t)) + (z_3(t) - z_1(t))]\} + \\ +(C_3 i_{mr}(u(t), t) + C_4)[(z_4(t) - z_2(t)) + (z_3(t) - z_1(t))] \end{aligned} \tag{5}$$

is the MR damper force represented by the hyperbolic tangent model with the parameters: C_1, C_2, C_3, C_4, ν [40]; $i_{mr}(u(t), t)$ is the MR damper control current, $F_a(t)$ is the actuator force, and $F_e(t)$ is the excitation force applied to the protected structure. To include the MR damper current restriction to $[0,\ i_{max}]$ range ($i_{max} > 0$), it was further assumed:

$$i_{mr}(u(t), t) = i_{max} \sin^2(u_1(t)). \tag{6}$$

To include the actuator output (static) nonlinearity, i.e., the nominal force limitation to $[-F_{nom},\ F_{nom}]$ range (see the adopted F_{nom} design values in Table 1), it was assumed:

$$F_a(t) = F_{nom} \sin(u_2(t)). \tag{7}$$

Remark

For an electric servo drive with a ball screw slide mechanism used as the force actuator in this study (see Section 5), the output was considered to be linear within limits of $[-F_{nom},\ F_{nom}]$ (contrary to the electro-hydraulic actuator considered in [34]); the corresponding motor driving torque range was $\left[-\frac{rF_{nom}}{\pi} - M_0, \frac{rF_{nom}}{\pi} + M_0\right]$, where M_0 is no-load driving torque of the slide unit, while r is the spindle radius. In addition to the actuator's static non-linearity (force limitation), its linear dynamics were not considered in this study.

The regarded quality function was:

$$\begin{aligned} g(z(t), u(t), t) = g_{11}{z_1}^2(t) + g_{12}{z_2}^2(t) + g_{13}(z_1(t) - z_3(t))^2 + g_{14}(z_2(t) - z_4(t))^2 + g_{21}{i_{mr}}^2(u(t), t) + \\ g_{221}{F_{mr}}^2(z(t), u(t), t) + g_{222}{F_a}^2(u(t)) + g_{23}{P_a}^2(u(t)) \end{aligned} \tag{8}$$

to account for the protected structure displacement z_1 and velocity z_2 minimisation, the TVA stroke $z_1 - z_3$ minimisation, the MR damper coil current i_{mr} and resistance force F_{mr} minimisation, and the actuator force F_a and power P_a minimisation, where:

$$P_a(t) = F_a(t)(z_2(t) - z_4(t)).$$

Assume the Hamiltonian in the form:

$$H(\xi(t), z(t), u(t), t) = -g(z(t), u(t), t) + \xi^T(t) f(z(t), u(t), t). \tag{9}$$

If $(z^*(t), u^*(t))$ is an optimal control process, there exists a co-state vector function ξ satisfying the equation:

$$\dot{\xi}(t) = -f_z^{*T}(z^*(t), u^*(t), t)\xi(t) + g_z^T(z^*(t), u^*(t), t),\ t \in [t_0, t_1] \tag{10}$$

with a terminal (transversality) condition:

$$\xi(t_1) = 0 \tag{11}$$

so that $u^*(t)$ maximises the Hamiltonian over the set U for almost all $t \in [t_0, t_1]$ (f_z and g_z are f and g derivatives with respect to z; f and g are continuously differentiable with respect to state and continuous with respect to time and control) [56]. For the analysed system, the co-state vector was:

$$\xi(t) = [\xi_1(t)\ \ \xi_2(t)\ \ \xi_3(t)\ \ \xi_4(t)]^T, \tag{12}$$

while:

$$f_z^{*T}(z^*(t), u^*(t), t) = \begin{bmatrix} 0 & -\frac{1}{m_1}\left(k_1 + k_2 + \widetilde{F}_{mr}(z^*(t), u^*(t), t)\right) & 0 & \frac{1}{m_2}\left(k_2 + \widetilde{F}_{mr}(z^*(t), u^*(t), t)\right) \\ 1 & -\frac{1}{m_1}\left(c_1 + \widetilde{F}_{mr}(z^*(t), u^*(t), t)\right) & 0 & \frac{1}{m_2}\widetilde{F}_{mr}(z^*(t), u^*(t), t) \\ 0 & \frac{1}{m_1}\left(k_2 + \widetilde{F}_{mr}(z^*(t), u^*(t), t)\right) & 0 & -\frac{1}{m_2}\left(k_2 + \widetilde{F}_{mr}(z^*(t), u^*(t), t)\right) \\ 0 & \frac{1}{m_1}\widetilde{F}_{mr}(z^*(t), u^*(t), t) & 1 & -\frac{1}{m_2}\widetilde{F}_{mr}(z^*(t), u^*(t), t) \end{bmatrix} \tag{13}$$

with:

$$\begin{aligned} &\widetilde{F}_{mr}(z^*(t), u^*(t), t) = \\ &\nu(C_1 i_{mr}(u^*(t), t) + C_2)\left\{1 - \tanh^2\left[\nu\left(z_4^*(t) + z_3^*(t) - z_2^*(t) - z_1^*(t)\right)\right]\right\} + +(C_3 i_{mr}(u^*(t), t) + C_4) \end{aligned} \tag{14}$$

thus:

$$\begin{aligned} &\widetilde{F}_{mr}(z^*(t), u^*(t), t) = \\ &\frac{\partial F_{mr}(z^*(t), u^*(t), t)}{\partial z_3^*(t)} = \frac{\partial F_{mr}(z^*(t), u^*(t), t)}{\partial z_4^*(t)} = -\frac{\partial F_{mr}(z^*(t), u^*(t), t)}{\partial z_1^*(t)} = -\frac{\partial F_{mr}(z^*(t), u^*(t), t)}{\partial z_2^*(t)} \end{aligned} \tag{15}$$

and:

$$\begin{aligned} &g_z^T(z^*(t), u^*(t), t) \\ &= \begin{bmatrix} 2g_{11}z_1^*(t) + 2g_{13}\left(z_1^*(t) - z_3^*(t)\right) - 2g_{221}F'_{mr}(z^*(t), u^*(t), t) \\ 2g_{12}z_2^*(t) + 2g_{14}\left(z_2^*(t) - z_4^*(t)\right) - 2g_{221}F'_{mr}(z^*(t), u^*(t), t) + 2g_{23}F_a^2(t)\left(z_2^*(t) - z_4^*(t)\right) \\ -2g_{13}\left(z_1^*(t) - z_3^*(t)\right) + 2g_{221}F'_{mr}(z^*(t), u^*(t), t) \\ -2g_{14}\left(z_2^*(t) - z_4^*(t)\right) + 2g_{221}F'_{mr}(z^*(t), u^*(t), t) - 2g_{23}F_a^2(t)\left(z_2^*(t) - z_4^*(t)\right) \end{bmatrix} \end{aligned} \tag{16}$$

where:

$$F'_{mr}(z^*(t), u^*(t), t) = F_{mr}(z^*(t), u^*(t), t)\widetilde{F}_{mr}(z^*(t), u^*(t), t).$$

Thus, Hamiltonian (9) takes a form:

$$\begin{aligned} H(\xi(t), z(t), u(t), t) = &-g_{11}{z_1}^2(t) - g_{12}{z_2}^2(t) - g_{13}(z_1(t) - z_3(t))^2 - g_{14}(z_2(t) - z_4(t))^2 - \\ &g_{21}{i_{mr}}^2(u(t), t) - g_{221}{F_{mr}}^2(z(t), u(t), t) - g_{222}{F_a}^2(u(t)) - g_{23}{F_a}^2(u(t))(z_2(t) - z_4(t))^2 + \\ &\xi^T(t) f(z(t), u(t), t), \end{aligned}$$

where:

$$\xi^T(t)f(z(t),u(t),t)$$
$$= \begin{bmatrix} \xi_1(t) & \xi_2(t) & \xi_3(t) & \xi_4(t) \end{bmatrix} \begin{bmatrix} z_4(t) \\ \frac{1}{m_1}(-(k_1+k_2)z_1(t) - c_1 z_2(t) + k_2 z_3(t) + F_{mr}(z(t),u(t),t) + F_a(u(t)) + F_e(t)) \\ z_4(t) \\ \frac{1}{m_2}(k_2 z_1(t) - k_2 z_3(t) - F_{mr}(z(t),u(t),t) - F_a(u(t))) \end{bmatrix}$$

The Hamiltonian maximisation conditions [56] are:

$$\frac{\partial H(\xi(t),z^*(t),u(t),t)}{\partial u_1(t)} = \left\{ \left(\frac{1}{m_1}\xi_2(t) - \frac{1}{m_2}\xi_4(t) - 2g_{221}F_{mr}(z^*(t),u(t),t) \right) \frac{\partial F_{mr}(z^*(t),u(t),t)}{\partial i_{mr}(u(t),t)} - 2i_{\max g21}\sin^2(u_1(t)) \right\} \sin(2u_1(t))i_{\max} = 0 \quad (17)$$

$$\frac{\partial H(\xi(t),z^*(t),u(t),t)}{\partial u_2(t)} = \left\{ \frac{1}{m_1}\xi_2(t) - \frac{1}{m_2}\xi_4(t) - 2F_{nom}\left[g_{222} + g_{23}(z_2(t) - z_4(t))^2 \right] \sin(u_2(t)) \right\} \cos(u_2(t))F_{nom} = 0 \quad (18)$$

with the appropriate sign change regimes, where:

$$\frac{\partial F_{mr}(z^*(t),u(t),t)}{\partial i_{mr}(u(t),t)} = C_1 \tanh[\nu(z_4^*(t) + z_3^*(t) - z_2^*(t) - z_1^*(t))] + C_3(z_4^*(t) + z_3^*(t) - z_2^*(t) - z_1^*(t))$$

Let us fix an attention on $u_1(t)$ range of $[0,\ \pi]$; thus, Equation (17) results in ($g_{21} \neq 0$ is assumed):

$$\sin(2u_1(t)) = 0$$

or:

$$\sin^2(u_1(t)) = \frac{1}{2i_{\max_{21}}} \left(\frac{1}{m_1}\xi_2(t) - \frac{1}{m_2}\xi_4(t) - 2g_{221}F_{mr}(z^*(t),u(t),t) \right) \frac{\partial F_{mr}(z^*(t),u(t),t)}{\partial i_{mr}(u(t),t)} a \quad (19)$$

Analogically to [31]:

$$i_{mr}^*(u^*(t),t) = \begin{cases} \frac{1}{2g_{21}} \left(\frac{1}{m_1}\xi_2(t) - \frac{1}{m_2}\xi_4(t) - 2g_{221}F_{mr}(z^*(t),u(t),t) \right) \frac{\partial F_{mr}(z^*(t),u(t),t)}{\partial i_{mr}(u(t),t)}, & 0,\ if,\ RHS(19) < 0 \\ & if\ RHS(19) \in [0\ 1) \\ & i_{\max},\ if\ RHS(19) \in \geq 1 \end{cases} \quad (20)$$

where $RHS(19)$ is the right-hand side of Equation (19).

Condition (18) yields ($g_{222} \neq 0$ is assumed):

$$\frac{\partial H(\xi(t),z^*(t),u(t),t)}{\partial u_2(t)} = \left\{ \frac{1}{2F_{nom}\left[g_{222} + g_{23}(z_2(t) - z_4(t))^2 \right]} \left(\frac{1}{m_1}\xi_2(t) - \frac{1}{m_2}\xi_4(t) \right) - \sin(u_2(t)) \right\} \cos(u_2(t)) = 0. \quad (21)$$

To analyse Hamiltonian derivative (21) sign change conditions, let us fix an attention on $u_2(t)$ range of $[-\pi, \pi\ ]$, regarding the period of both $\sin(u_2(t))$ and $\cos(u_2(t))$. This analysis, with the help of Figure 3, yielded proposition (22)(23)(24), covering three disjoint and complementary cases:

(1) *if* $\left\{ \frac{1}{2F_{nom}\left[g_{222} + g_{23}(z_2(t) - z_4(t))^2 \right]} \left(\frac{1}{m_1}\xi_2(t) - \frac{1}{m_2}\xi_4(t) \right) \right\} \leq -1$, *then* (21) is fulfilled and $\frac{\partial H(\xi(t),z^*(t),u(t),t)}{\partial u_2(t)}$ exhibits $+/-$ sign change (Hamiltonian maximisation) for: ${u_2}^*(t) = -\frac{\pi}{2}$ only (see Figure 3); *thus*:

$$F_a^*(t) = -F_{nom}. \quad (22)$$

(2) *if* $\left\{ \frac{1}{2F_{nom}\left[g_{222}+g_{23}(z_2(t)-z_4(t))^2\right]}\left(\frac{1}{m_1}\xi_2(t)-\frac{1}{m_2}\xi_4(t)\right)\right\} \geq 1$, *then* (21) is fulfilled and $\frac{\partial H(\xi(t),z^*(t),u(t),t)}{\partial u_2(t)}$ exhibits $+/-$ sign change (Hamiltonian maximisation) for: ${u_2}^*(t)=\frac{\pi}{2}$ only (see Figure 3); *thus*:

$$F_a^*(t)=F_{nom}. \tag{23}$$

(3) *if* $\left\{ \frac{1}{2F_{nom}\left[g_{222}+g_{23}(z_2(t)-z_4(t))^2\right]}\left(\frac{1}{m_1}\xi_2(t)-\frac{1}{m_2}\xi_4(t)\right)\right\} \in (-1,\,1)$, *then* (21) is fulfilled and $\frac{\partial H(\xi(t),z^*(t),u(t),t)}{\partial u_2(t)}$ exhibits $+/-$ sign change (Hamiltonian maximisation) for: ${u_2}^*(t)=\arcsin\left\{ \frac{1}{2F_{nom}\left[g_{222}+g_{23}\left(z_2^*(t)-z_4^*(t)\right)^2\right]}\left(\frac{1}{m_1}\xi_2(t)-\frac{1}{m_2}\xi_4(t)\right)\right\}$ only (see Figure 3); thus:

$$F_a^*(t)=\frac{1}{2\left[g_{222}+g_{23}\left(z_2^*(t)-z_4^*(t)\right)^2\right]}\left(\frac{1}{m_1}\xi_2(t)-\frac{1}{m_2}\xi_4(t)\right) \tag{24}$$

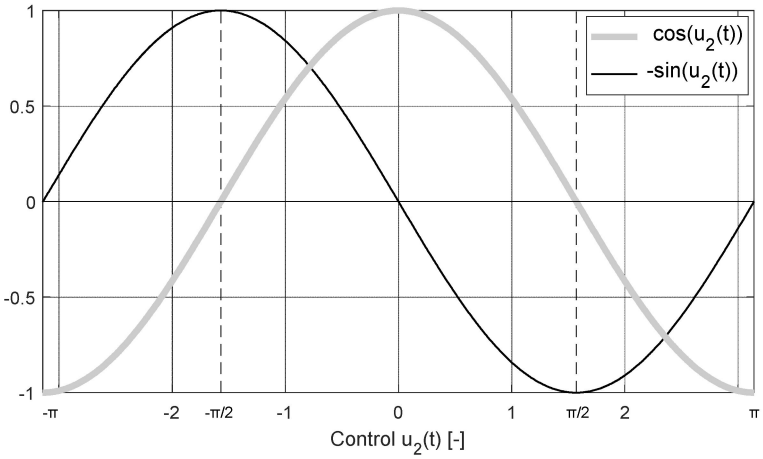

Figure 3. Hamiltonian derivative (21) sign analysis.

4. Control Implementation

Regarding the considerations presented in [34,40,41], the implementation of the above control proposition (20) and (22)–(24) may be as follows: the boundary value problem (1)(3)(9)÷(11) may be solved in every sampling step of the real-time control, while the horizon of the optimisation may be assumed as one integration step to cope with the large computational load. A numerical implementation of such a nonlinear optimal control for a structure equipped with either an MR-TVA (a standard TVA featuring an MR damper instead of a passive one) [40] or an H-TVA [34] was realised recently using MATLAB/Simulink level-2 s-function and *bvp4c* iterative scheme [57]; it was shown numerically (for the MR-TVA system also experimentally [41]) that the iteration procedure yielding high computational load may be omitted, adopting a short time horizon optimal problem task and zero initial conditions for co-state integrators. It was proved that the influence of the terminal condition (11) error was negligible for the considered control applications. In the present research, both the active electric actuator optimal-based control and the

MR damper optimal-based control were implemented simultaneously in the TVA system (Figure 1)—this solution will be designated hereinafter by *OPT*.

A modified two-level displacement ground-hook control (hereinafter designated by *GH*)—the optimal control direct implementation for the case when the protected structure deflection minimisation is the single objective—was additionally regarded during this study. The *GH* control law changes the actuator force between $-F_{nom}$ and $+F_{nom}$ with regard to x_1 sign changes and varies the MR damper control current between 0 and i_{max}th regard to x_1 and F_{mr} signs [34,40].

On the experimental ground, the *OPT* approach was compared with the *GH* technique for different levels of the nominal actuator force and maximum MR damper current, adopting the 1 ms sampling step.

5. The Experimental Setup

The regarded wind turbine tower-nacelle scaled laboratory model fulfilled a dynamic similarity condition of motions of tower tips with a real-world full-scale wind turbine Vensys82 structure [49,50,53,54].

The test rig (Figure 4) consisted of a vertically oriented Ti-Gr5 circular rod (no. 1, modelling the wind turbine tower) and a complex of steel plates (no. 2, modelling the nacelle unit, including the turbine) fastened to the top of the rod, with the H-MR-TVA system built-in. The Ti-Gr5 rod was fixed to a section steel foundation frame (no. 3). The H-MR-TVA (no. 4) consisted of an additional mass moving horizontally along linear bearing guides, joined to the nacelle-unit (no. 2) via springs (no. 5), Lord RD-1097-1 MR damper (no. 6) [45], and Festo EGSC-BS-KF-32-50-8P mini slide actuator of linear stroke (powered by Festo EMME-AS-40-S-LV-AS servo motor) (no. 7) [58] in parallel. The H-MR-TVA operated along the same direction as the force excitation applied. The structure was excited by the TMS2060E modal shaker (no. 8 [59]), whose force was transferred to the nacelle-unit (no. 2) with the use of the drive train system (no. 9) of the changeable leverage.

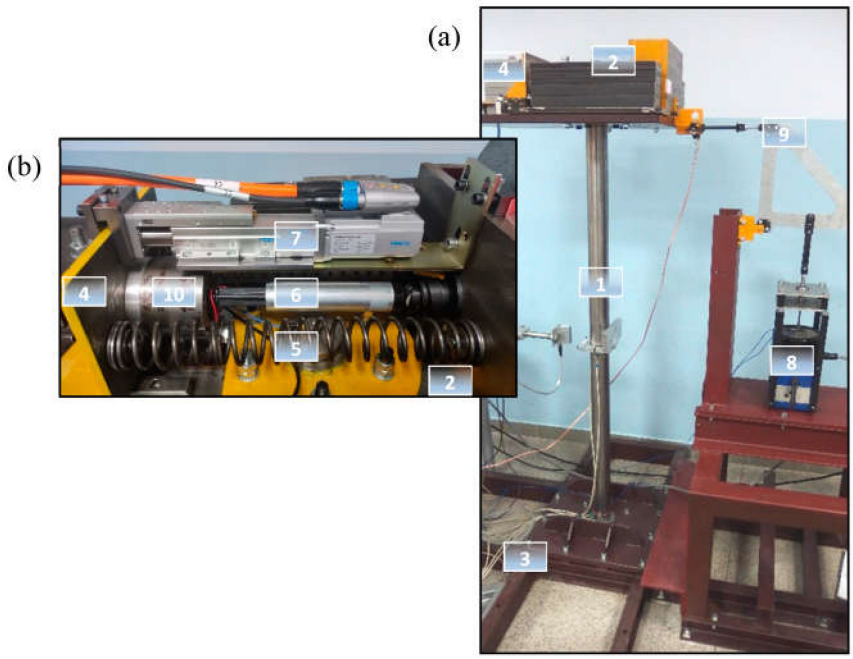

Figure 4. The laboratory test rig: (**a**) a general view, (**b**) the H-MR-TVA.

The data acquisition and control system used a laser sensor for the nacelle-unit absolute displacement (i.e., the tower tip deflection) x_1 measurement, a laser vibrometer for the H-MR-TVA mass absolute displacement x_2 measurement, the MR damper force sensor (no. 10), the shaker force sensor, the MR damper coil current Hall sensor, power supply and conditioning circuits for the sensors and actuators, and a measuring-control PC embedded

with Inteco I/O board of the RT-DAC4 series [60] and MATLAB/Simulink/RT-CON applications. The RT-CON software ensured the fulfilment of real-time regimes using the 1 kHz sampling rate. The RT-DAC4 analogue input channels and RT-CON analogue input drivers mediated measurement data transfer to the Simulink control environment, where the demanded MR damper current/actuator force was calculated in each sample step. The RT-CON/RT-DAC4 analogue output drivers/channels were used for control output mediation. The MR damper current output was conditioned with the dedicated amplifier and PID controller to force the required electric current through the MR damper coil. The demanded actuator force was fed to the Festo CMMT-AS-C2-3A-EC-S1 servo controller connected with the EMME-AS-40-S-LV-AS motor. The shaker control output was generated using the TMS2060E force measurement signal compared with the demanded excitation pattern and conditioned with the PI controller implemented in the MATLAB/Simulink/RT-CON environment [36].

The system parameters, as in Table 1, along with the identified MR damper unit (Table 2) [41] and electric drive (21) parameters, were assumed for the experiments.

Table 2. The identified MR damper unit parameters [41].

Parameter	Value
C_1	44
C_2	1.0
C_3	225
C_4	7.0
ν	70

The electric drive ±15 N step response series was gathered (Figure 5) using the locked (with 0.9 A control current) MR damper, built-in parallel, and its force sensor (no. 10, Figure 4). The response was identified with a time-delayed transfer Function (21) of three poles and two zeros from MATLAB *System Identification App* (fit to estimation data 96%, data prefiltered, stability enforced):

$$G_a(s) = \frac{32.6s^2 + 1.55e4s + 9.66e4}{s^3 + 140s^2 + 1.71e4s + 1.06e5} e^{-0.006s} \tag{25}$$

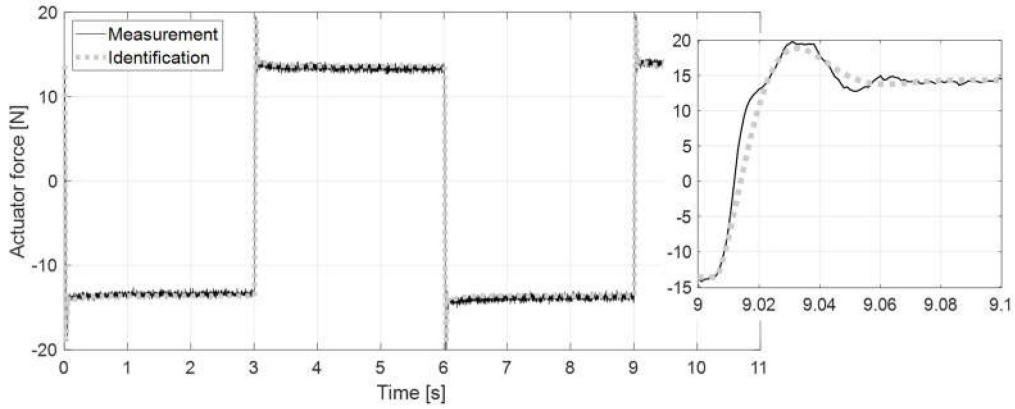

Figure 5. Electric drive force step response series: measurement vs. identification.

The actuator identification tests confirmed the considerable response delay of the used mini slide powered by a servo motor (the electro-hydraulic cylinder assumed in the previous numerical study [34] guaranteed a measurably faster response [61]), which was projected to be compensated by the MR damper output force (exhibiting a few-millisecond response time) while maintaining the simplicity of real-time hardware implementation—

the electric drive response delay influenced state and co-state variables values, which in turn amended the i^*_{mr} control current according to (20).

6. The Test Conditions

For the real-time vibration control of the wind turbine tower-nacelle model first bending mode, the approach described in Sections 3 and 4 was implemented using the damper control Formula (20) and the actuator control Formulas (22)–(24). Various *OPT* control *cases I–III* (see below) were regarded along with *GH* control, assuming different MR damper maximum currents and actuator nominal force values.

The test conditions parameters were as follows. The wind turbine tower-nacelle model was excited by a harmonic force of amplitude $A(F_e(t)) = 45.4$ N and a frequency range of $[2.2,\ 4.5]$ Hz. The fixed sample step $t_s = 10^{-3}$ s was adopted. The nominal actuator output force $F_{nom} = 12.5$ N (thus servo motor nominal driving torque $M_{nom} = 17.2{\cdot}10^{-3}$ Nm) was assumed as a *baseline OPT*/*GH* configuration, along with $F_{nom} = 6.25$ N assumed as its more energy-efficient, *restricted force* alternative; the corresponding actuator control signal $F_{a\ ctr}$ maximum value of 15 N for the *OPT* system (13.5 N for the *GH* system), or 7.5 N for the *OPT* system (6.75 N for the *GH* system) (see time responses in Section 7), were assumed accordingly, based on the identification (25). The maximum value of $F_{a\ ctr}$ corresponding to the assumed F_{nom} value for the *GH* system was 10% lower than for the *OPT* system due to the 10% duty cycle of the *OPT* resetting function (zero initial conditions for co-state integrators are assumed). The MR damper maximum current $i_{max} = 1.0$ as was assumed for the *baseline* configuration ($F_{nom} = 12.5$ N), while $i_{max} = 0.5$ as was assumed for its *restricted force* counterpart ($F_{nom} = 6.25$ N)—see Table 3. The values of i_{max} elding F_{mr} ranges were tuned to the assumed F_{nom} ranges, as the MR damper, due to its few-millisecond response time (see, e.g., Figure 12b in [41] p. 12), was activated ahead of the electric drive, while the electric actuator may have cancelled the detrimental MR damper remanent force.

Table 3. The test cases: nominal actuator force F_{nom}/maximum MR damper current *i_max*.

Configuration \ Control Method	***OPT CASE I*** $g_{221} = 0$ $g_{23} = 0$	***OPT CASE II*** $g_{221} = 10^6$ $g_{23} = 0$	***OPT CASE III*** $g_{221} = 0$ $g_{23} = 10^{10}$ ***or*** $g_{23} = 10^{11}$	***GH***
Baseline	12.5 N/1.0 A	12.5 N/1.0 A	12.5 N/1.0 A	12.5 N/1.0 A
Restricted force	6.25 N/0.5 A	6.25 N/0.5 A	6.25 N/0.5 A	6.25 N/0.5 A

The general weighting factors for the *OPT* control solution's quality index (8) were assumed as follows: $g_{11} = 10^{18}$, $g_{12} = 0$, $g_{13} = 10^{15}$, $g_{14} = 0$, $g_{21} = 4$, $g_{222} = 4{\cdot}10^{-12}$. A negligible but nonzero g_{222} value was selected to eliminate calculation problems for $z_2(t) = z_4(t)$ in (21), (22)(23)(24); the electric drive force magnitude was tuned through the F_{nom} assumption (*baseline* or *restricted force* configuration) in the current research.

The remaining weights were assumed to (*OPT cases I–III*, see Table 3):

I. minimise the primary structure deflection (nacelle-assembly displacement) x_1 amplitude as the primary objective while considering TVA stroke amplitude limitation (these were the two basic objectives for *cases II* and *III* as well);
II. minimise the MR damper force in addition to the *case I* objectives (to account for the MR damper's possible force limit and thermal constraints);
III. minimise the actuator power in addition to the *case I* objectives (to account for the actuator's energy constraints).

7. Real-Time Control Results

The efficiency of the adopted solutions was analysed using the frequency characteristics of the nacelle displacement (primary structure deflection) amplitude $A(x_1)$ (Figures 6–8), the TVA stroke amplitude $A(x_1 - x_2)$ (Figures 9–11), the maximum MR damper force (Figures 12–14), and the mean actuator power (Figures 15–17), along with the

time patterns of x_1, $x_1 - x_2$, $F_{a\ ctr}$, F_a, and F_{mr} (Figures 18–21). If omitted, $i_{max} = 0$ d all weights as for control *case I* (Section 6) were assumed all over this section. Figures 6, 9, 12 and 15 present the frequency characteristics of $A(x_1)$, $A(x_1 - x_2)$, the maximum MR damper force, and the mean actuator power, respectively, obtained for the *OPT* and *GH* systems with $F_{nom} = 12.5$ N, relative to the passive system with constant MR damper control current values of 0.0 A, 0.1 A, 0.2 A, 0.5 A, and idling electric actuator (passive system omitted in Figure 15). Similarly, Figures 7, 10, 13 and 16 present the frequency patterns of $A(x_1)$, $A(x_1 - x_2)$, the maximum MR damper force, and the mean actuator power, respectively, obtained for the *OPT* solution with $F_{nom} = 12.5$ N, and different i_{max}/g_{221} values ($i_{max} = 0$, $i_{max} = 0.5$ A or $i_{max} = 1.0$; nonzero MR damper force weight $g_{221} = 10^6$ for $i_{max} = 1.0$ case only), the *OPT* solution with $F_{nom} = 6.25$ N, and $i_{max} = 0$ $i_{max} = 0.5$ A, and *GH* solution with $F_{nom} = 6.25$ N, and $i_{max} = 0$ or $i_{max} = 0.5$ A. Additionally, Figures 8, 11, 14 and 17 present the frequency characteristics of $A(x_1)$, $A(x_1 - x_2)$, the maximum MR damper force, and the mean actuator power, respectively, obtained for the *OPT* concept with $F_{nom} = 12.5$ N and different i_{max}/g_{23} values ($i_{max} = 0$, $i_{max} = 0.5$ A or $i_{max} = 1.0$; the actuator power weight $g_{23} = 10^{10}$ or $g_{23} = 10^{11}$).

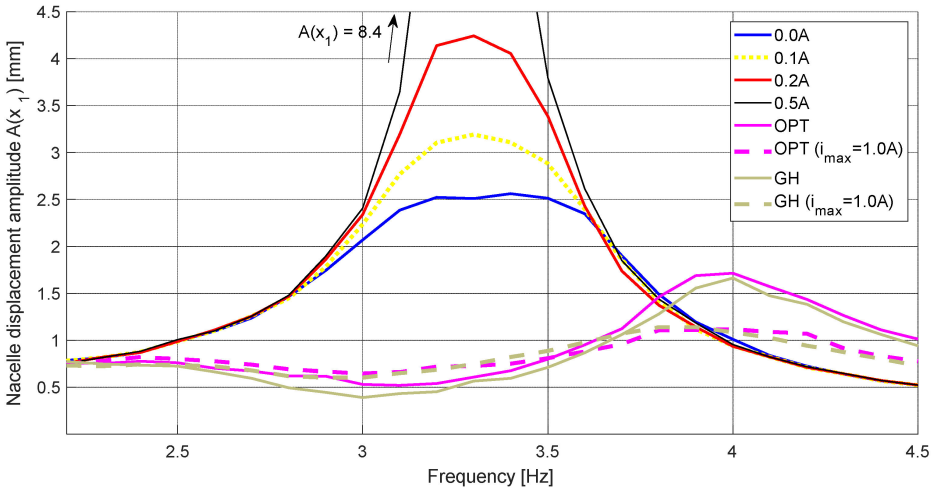

Figure 6. Nacelle horizontal displacement amplitude $A(x_1)$ frequency characteristics: passive system vs. *OPT* for $F_{nom} = 12.5$ N vs. *GH* for $F_{nom} = 12.5$ N.

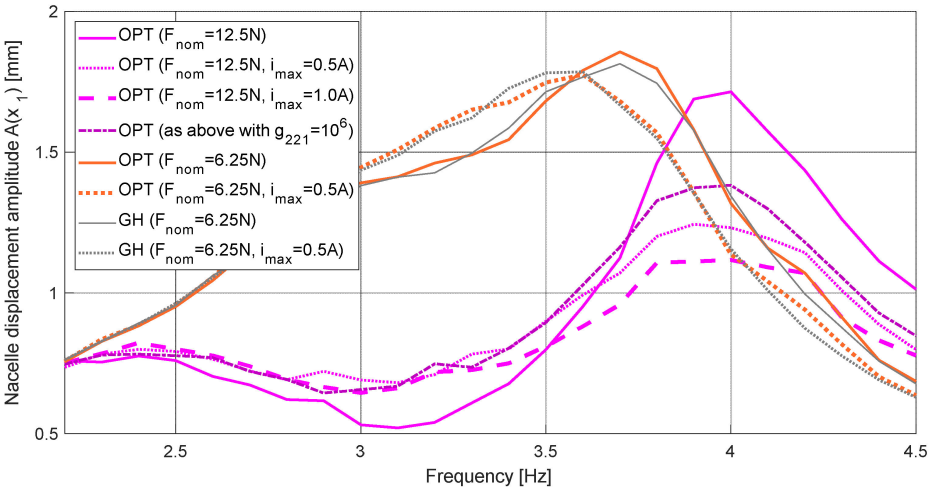

Figure 7. Nacelle horizontal displacement amplitude $A(x_1)$ frequency characteristics: *OPT* for different control parameter values vs. *GH* for $F_{nom} = 6.25$ N.

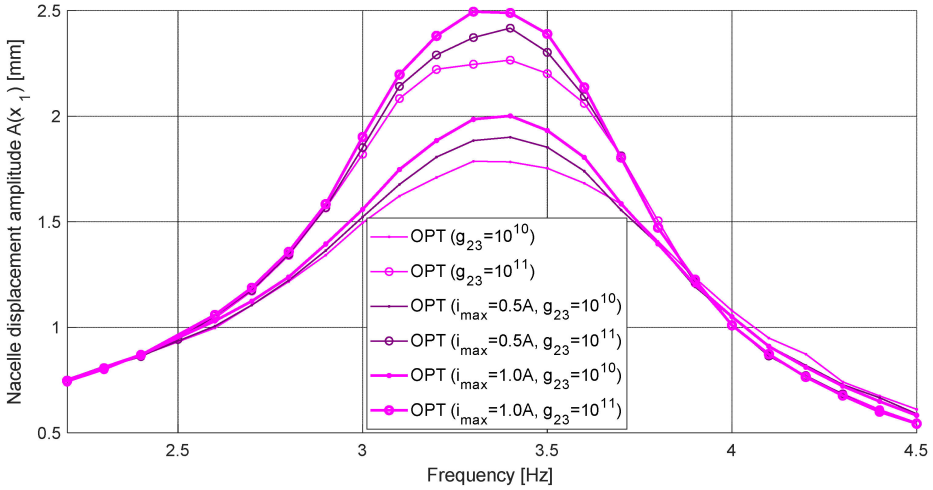

Figure 8. Nacelle horizontal displacement amplitude $A(x_1)$ frequency characteristics: *OPT* for different i_{max} d g_{23} values, and $F_{nom} = 12.5$ N.

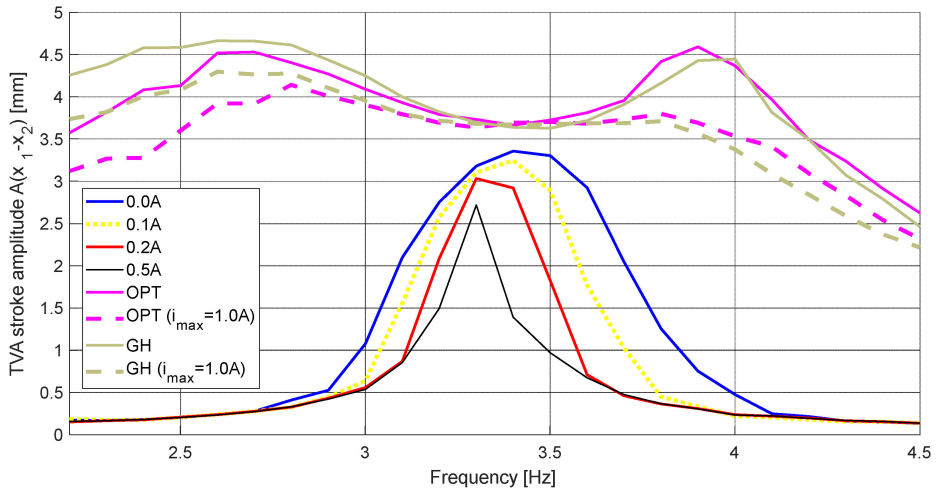

Figure 9. The TVA stroke amplitude $A(x_1 - x_2)$ frequency characteristics: passive system vs. *OPT* for $F_{nom} = 12.5$ N vs. *GH* for $F_{nom} = 12.5$ N.

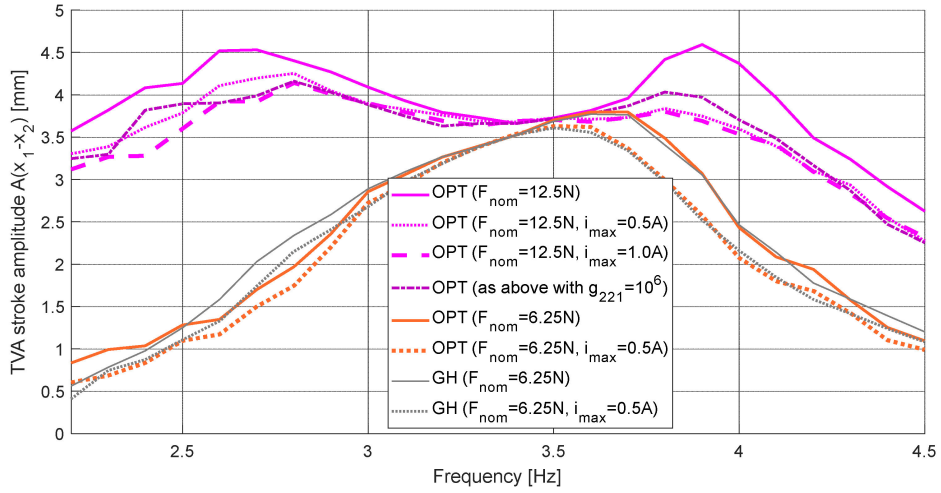

Figure 10. The TVA stroke amplitude $A(x_1 - x_2)$ frequency characteristics: *OPT* for different control parameter values vs. *GH* for $F_{nom} = 6.25$ N.

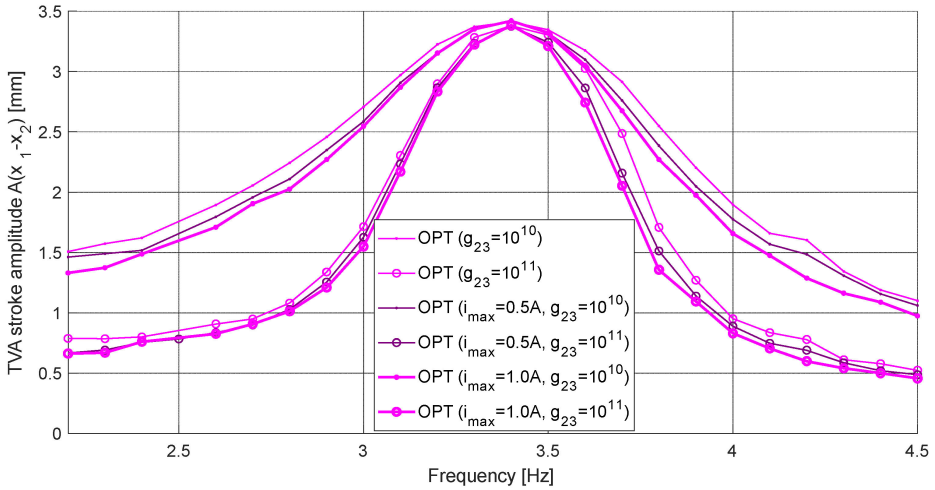

Figure 11. The TVA stroke amplitude $A(x_1 - x_2)$ frequency characteristics: *OPT* for different i_{max} an d g_{23} values, and $F_{nom} = 12.5$ N.

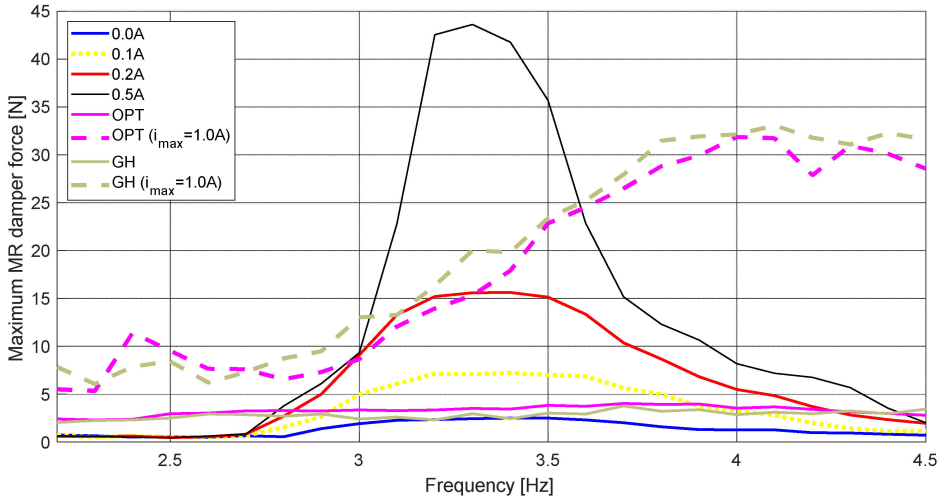

Figure 12. The maximum MR damper force frequency characteristics: passive system vs. *OPT* for $F_{nom} = 12.5$ N vs. *GH* for $F_{nom} = 12.5$ N.

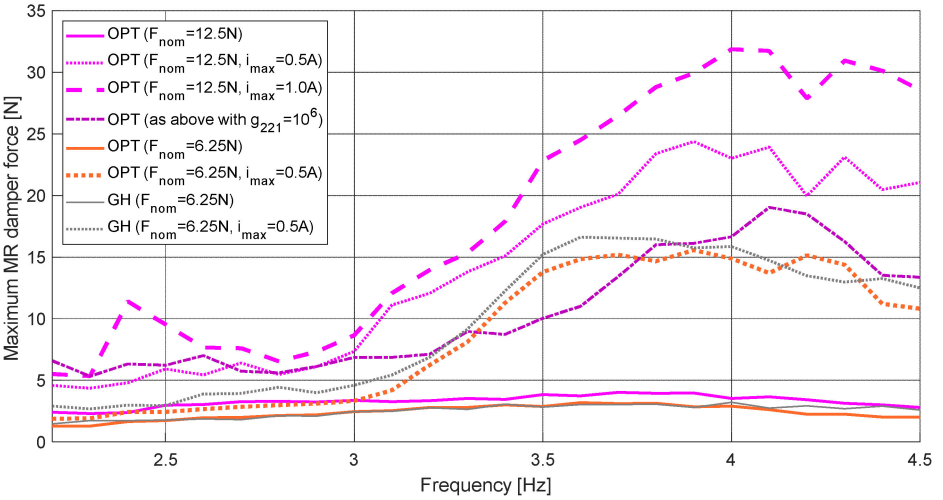

Figure 13. The maximum MR damper force frequency characteristics: *OPT* for different control parameter values vs. *GH* for $F_{nom} = 6.25$ N.

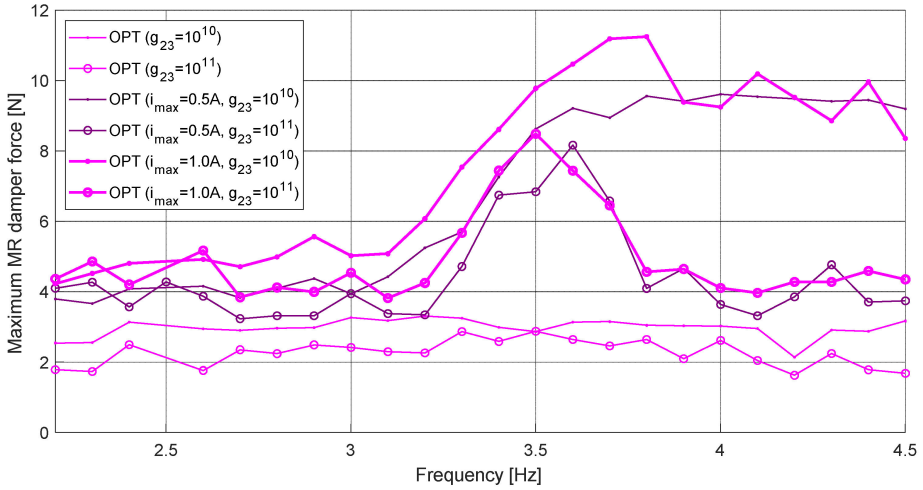

Figure 14. The maximum MR damper force frequency characteristics: *OPT* for different i_{max} and g_{23} values, and $F_{nom} = 12.5$ N.

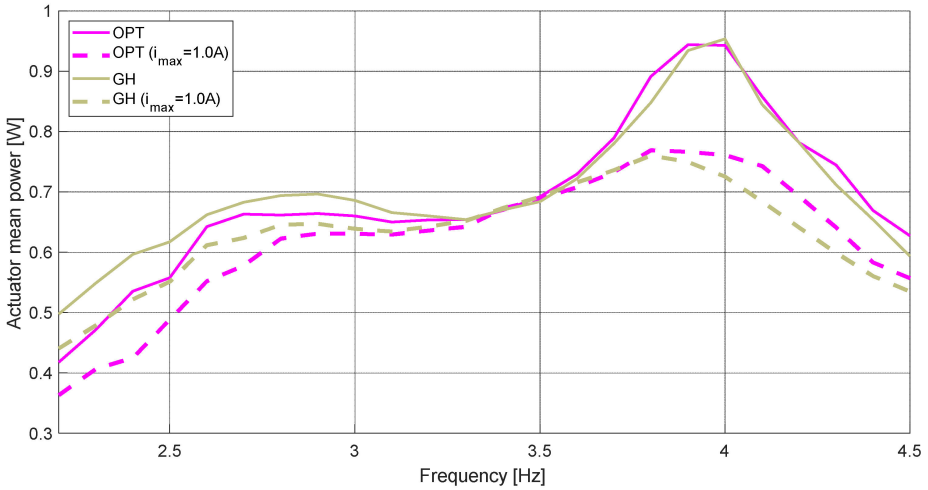

Figure 15. The mean actuator power frequency characteristics: *OPT* for $F_{nom} = 12.5$ N vs. *GH* for $F_{nom} = 12.5$ N.

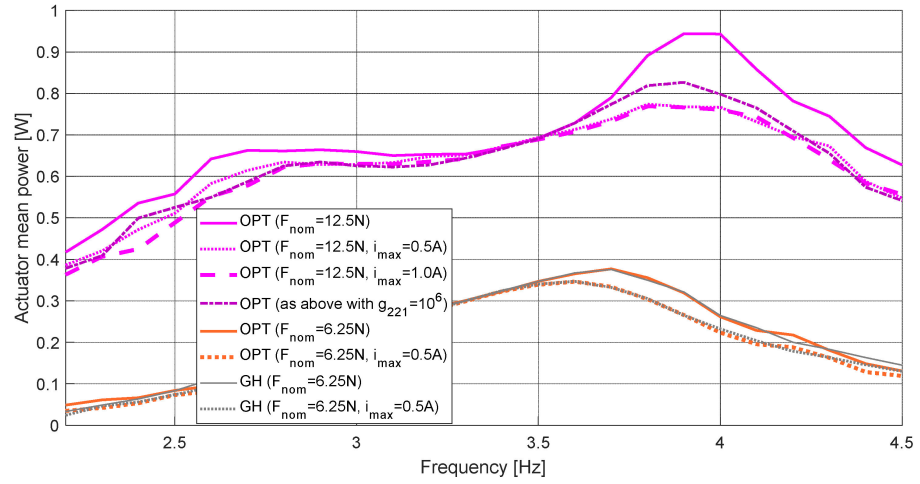

Figure 16. The mean actuator power frequency characteristics: *OPT* for different control parameter values vs. *GH* for $F_{nom} = 6.25$ N.

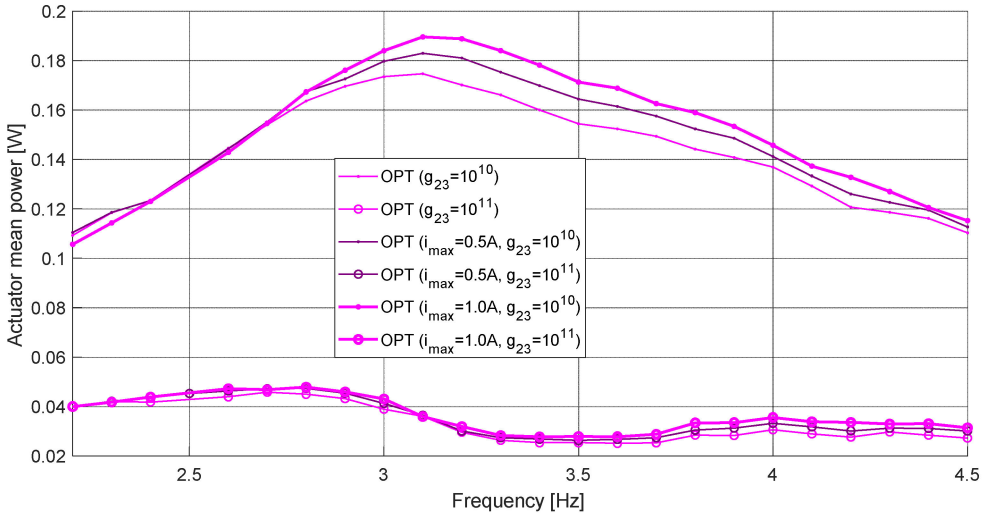

Figure 17. The mean actuator power frequency characteristics: *OPT* for different i_{max} and g_{23} values, and $F_{nom} = 12.5$ N.

Figures 18–21 present the comparison of the primary structure deflection (i.e., nacelle horizontal displacement) x_1, the TVA displacement $x_1 - x_2$, the actuator control signal $F_{a\ ctr}$ and force F_a, and the MR damper force F_{mr} time patterns obtained at the specific frequency points: 3.2 Hz (Figure 18), 4.0 Hz (Figure 19), 3.4 Hz (Figure 20), 3.6 Hz, and 3.7 Hz (Figure 21). Figures 18 and 19 present the comparison of the time responses obtained for the *OPT* system with $F_{nom} = 12.5$ N, $i_{max} = 0/0.5/1.0$ A, $g_{221} = 0$, the *OPT* system with $F_{nom} = 12.5$ N, $i_{max} = 1.0$ A, $g_{221} = 10^6$, and the *GH* system with $F_{nom} = 12.5$ N, $i_{max} = 0/1.0$ A. Fig. 20 presents the comparison of the time responses obtained for the *OPT* system with $F_{nom} = 6.25$ N, and $i_{max} = 0$ or 0.5 A. Figure 21 compares the time responses determined for the *OPT* system with $F_{nom} = 12.5$ N, $i_{max} = 0/1.0$ A, and $g_{23} = 0/10^{10}/10^{11}$.

As may be observed in Figures 6 and 7 for $F_{nom} = 12.5$ N (in Figure 7 for $F_{nom} = 6.25$ N), both *OPT* and *GH* solutions with an MR damper semi-active operation (i.e., with nonzero $i_{\max}$) exhibited significantly lower maximum $A(x_1)$ values within the regarded structure first bending mode frequency neighbourhood (especially in 4.0 Hz neighbourhood), than *OPT* and *GH* without the MR damper support (i.e., with $i_{max} = 0$, omitted in the legends). The latter, however, presented slightly lower $A(x_1)$ values in the 3.2 Hz neighbourhood. These phenomena are illustrated in Figures 18 and 19 for $F_{nom} = 12.5$ N and various i_{max}/g_{221} values. The additional force provided by the MR damper semi-active operation resulted in a slightly smaller TVA stroke $(x_1 - x_2)$ amplitude (compared to Figures 9 and 10), which yielded somewhat lower TVA efficiency for nonzero i_{max} at 3.2 Hz (Figure 18). At a higher frequency of 4.0 Hz (Figure 19), however, the other factor was dominant in relation to the electric servo activation delay time regarding the shorter vibration period; thus, the MR damper few-millisecond response time was greatly beneficial, as previously expected (Section 5). Similar phenomena for $F_{nom} = 6.25$ N are depicted in Figure 20a,b (for 3.6 Hz) and Figure 20c,d (for 3.7 Hz). Figure 6 clearly indicates the TVA excess damping with regard to the optimally tuned TVA [19]—the maximum $A(x_1)$ for the zero-control passive system was greater than 2.5 mm. In contrast, Figure 2 suggests a value of 2.1 mm for a 14.1% mass ratio.

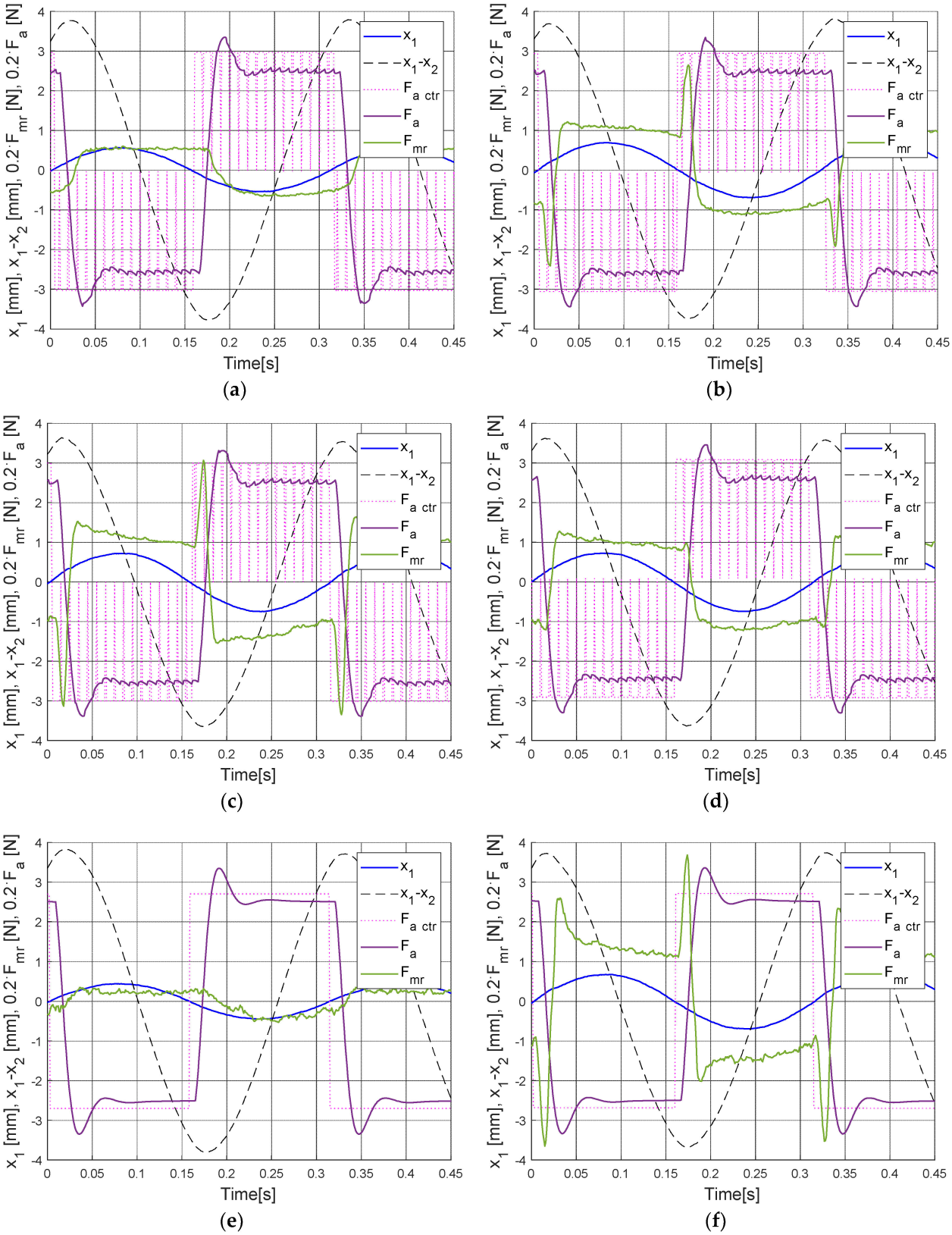

Figure 18. Time responses at 3.2 Hz: (**a**) *OPT*, $i_{max} = 0$ (**b**) *OPT*, $i_{max} = 0.5$ A (**c**) *OPT*, $i_{max} = 1.0$ A, (**d**) *OPT*, $i_{max} = 1.0$ A, $g_{221} = 10^6$, (**e**) *GH*, $i_{max} = 0$, (**f**) *GH*, $i_{max} = 1.0$ A ($F_{nom} = 12.5$ N).

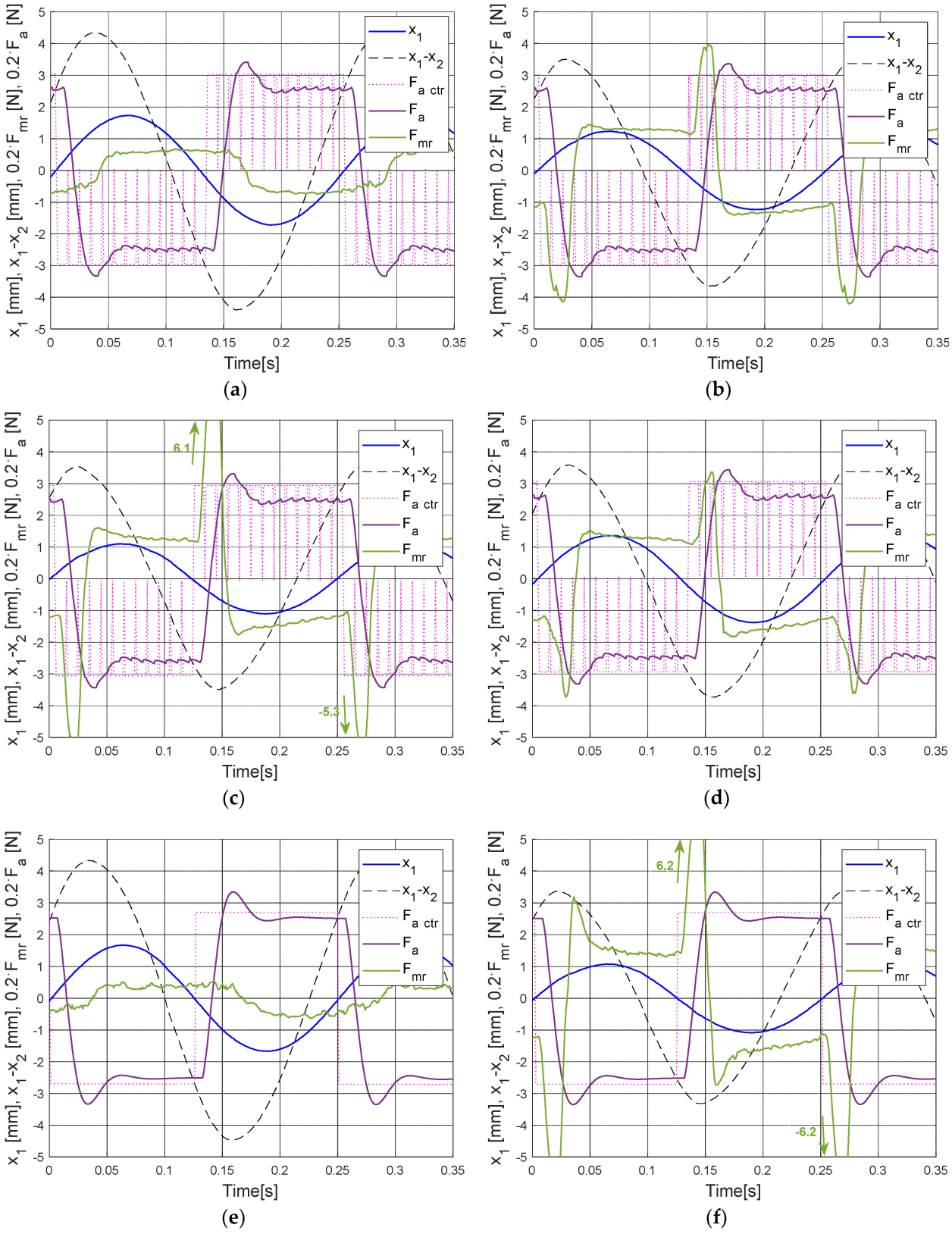

Figure 19. Time responses at 4.0 Hz: (**a**) *OPT*, $i_{max} = 0$ (**b**) *OPT*, $i_{max} = 0.5$ A (**c**) *OPT*, $i_{max} = 1.0$ A, (**d**) *OPT*, $i_{max} = 1.0$ A, $g_{221} = 10^6$, (**e**) *GH*, $i_{max} = 0$, (**f**) *GH*, $i_{max} = 1.0$ A ($F_{nom} = 12.5$ N).

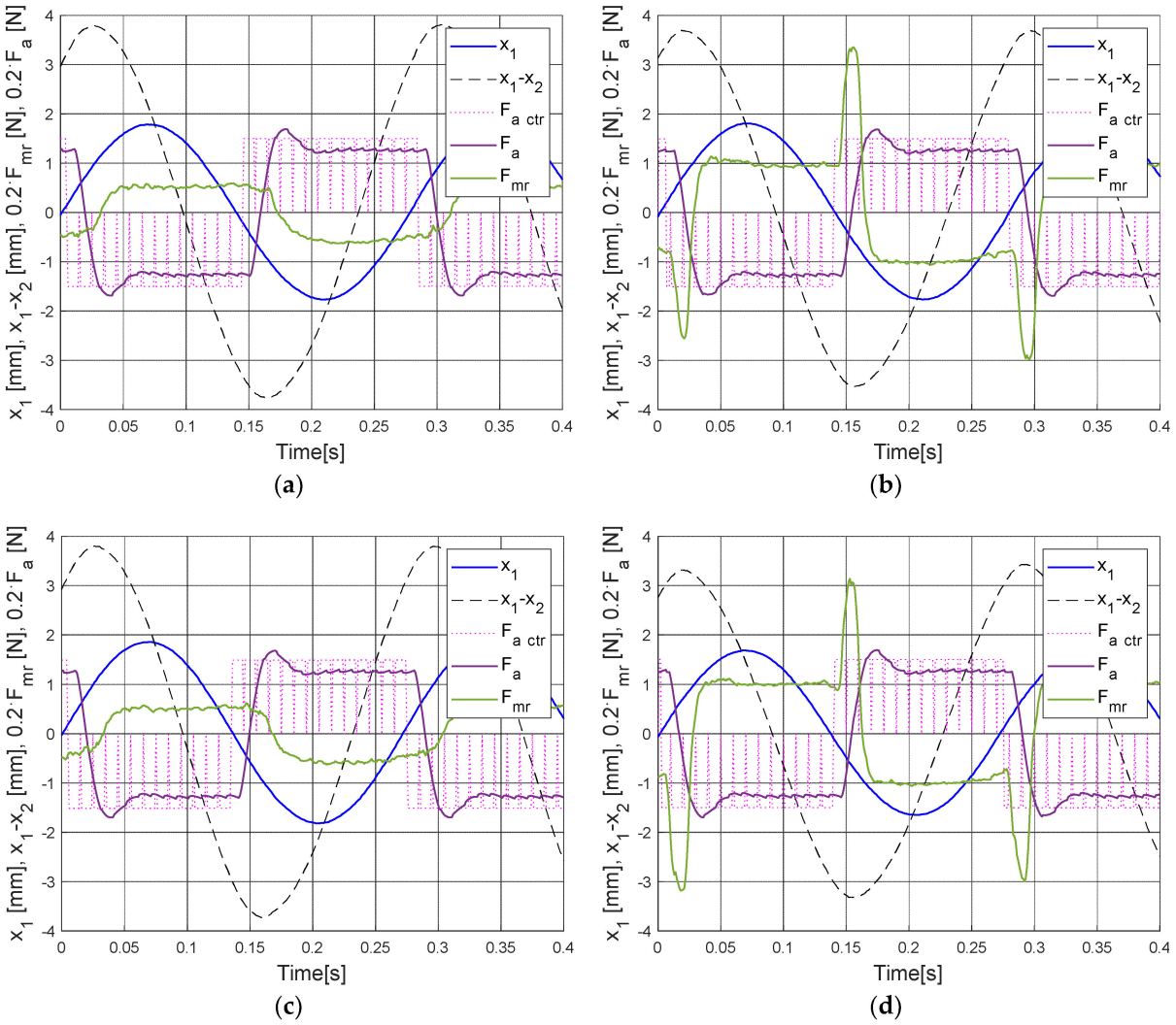

Figure 20. *OPT* time responses at 3.6 Hz: (**a**) $i_{max} = 0$, (**b**) $i_{max} = 0.5$ A vs. *OPT* time responses at 3.7Hz: (**c**) $i_{max} = 0$, (**d**) $i_{max} = 0.5$ A ($F_{nom} = 6.25$ N).

The combined electric drive and MR damper operation in the H-MR-TVA system (control *case I*, *baseline* configuration), i.e., with $F_{nom} = 12.5$ N, $i_{max} = 1.0$ A led to a 35% maximum $A(x_1)$ reduction in relation to the H-MR-TVA operation without MR damper semi-active support (i.e., with $i_{max} = 0$ a and 52% reduction with regard to the previous research with an MR-TVA system of a lower (7.7%) mass ratio, but less TVA excess damping [41]. This is regarded as a satisfactory result for such a real-time implementation, considering the nonlinearity of Figure 2 characteristics and the expected 23% $A(x_1)$ reduction only (Section 2). Both *GH* and *OPT* (control *case I*, *baseline* configuration) provided maximum $A(x_1)$ values close to 1.1 mm (i.e., 57% reduction concerning the 0.0 A passive configuration exhibiting the lowest $A(x_1)$ values, and 87% reduction regarding the 0.5 A passive configuration, see Figure 6). This result was obtained at ca. 4 mm TVA stroke amplitude (*OPT* configuration, Figure 9), ca. 32 N maximum MR damper force (Figure 12), and ca. 0.76 W maximum actuator power (Figure 15). The configurations without the MR damper semi-active support were characterised by more than 4.5 mm TVA stroke amplitude, only 4 N maximum MR damper force, and as much as 0.95 W maximum actuator power, while being significantly less efficient in primary structure deflection minimisation.

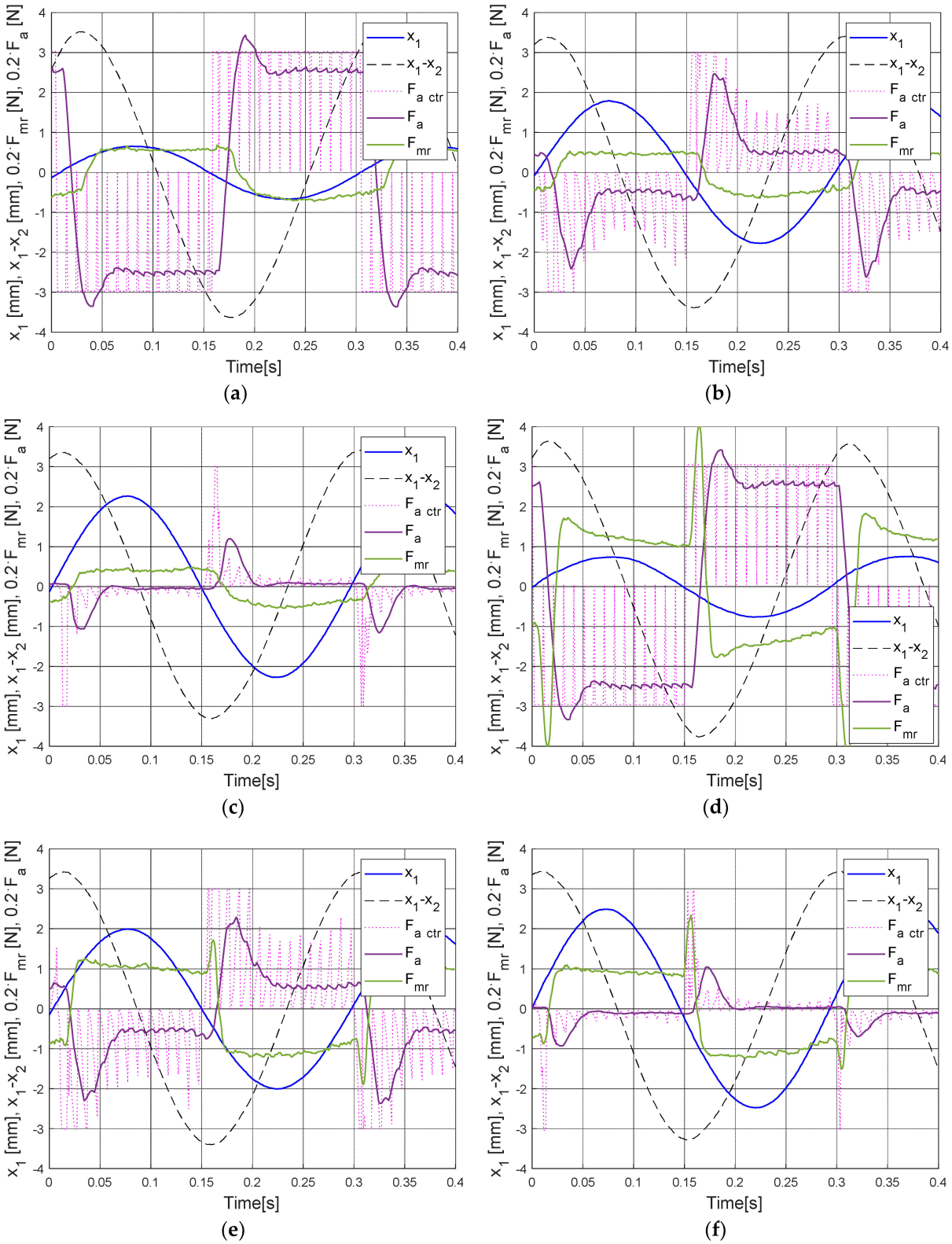

Figure 21. *OPT* time responses at 3.4 Hz: (**a**) $i_{max} = 0$ (**b**) $i_{max} = 0$, $g_{23} = 10^{10}$ (**c**) $i_{max} = 0$, $g_{23} = 10^{11}$ (**d**) $i_{max} = 1.0$ A (**e**) $i_{max} = 1.0$ A, $g_{23} = 10^{10}$, (**f**) $i_{max} = 1.0$ A, $g_{23} = 10^{11}$ ($F_{nom} = 12.5$ N).

As presented in Figures 6, 9, 12 and 15 for $F_{nom} = 12.5$ N (in Figures 7, 10, 13 and 16 for $F_{nom} = 6.25$ N), the results of *OPT* and *GH* operation were similar, with minor differences noticeable concerning $A(x_1)$, $A(x_1 - x_2)$, the maximum MR damper force, and the mean actuator power, especially for $F_{nom} = 12.5$ N. In Figure 18a,c vs. Figure 18e,f as well as

in Figure 19a,c vs. Figure 19e,f, disparities in the time patterns may be spotted with $F_{a\ ctr}$ differences coming to the forefront, as explained in the final paragraph of Section 6.

The interesting alternative to the *baseline* configuration ($F_{nom} = 12.5$ N, $i_{max} = 1.0$ A with $g_{221} = 0$ (control *case I*) was a configuration with a lower $i_{max} = 0.5$ A value (control *case I*), and with $i_{max} = 1.0$ A and nonzero MR damper force weight $g_{221} = 10^6$ (control *case II*); $F_{nom} = 12.5$ N for both these configurations. In Figures 7, 10, 13 and 16, the respective frequency characteristics are included, while in Figure 18b,d as well as in Figure 19b,d, the time patterns are presented. It may be observed that these two solutions exhibited higher x_1 deflection amplitudes, similar $x_1 - x_2$ strokes, and lower MR damper forces (as intended, especially for the $i_{max} = 1.0$ A, $g_{221} = 10^6$ configuration) than the *baseline* configuration. The maximum actuator power used in the $i_{max} = 1.0$ A, $g_{221} = 10^6$ configuration was actually slightly higher, being also less efficient in $A(x_1)$ minimisation than the $i_{max} = 0.5$ A, $g_{221} = 0$ configuration. In Figure 18c vs. Figure 18d as well as in Figure 19c vs. Figure 19d, the differences in the F_{mr} patterns resulting from the different g_{221} (MR damper force) weights may be spotted. Due to the MR damper millisecond response time, its control signal i_{mr} patterns were omitted in the time characteristics Figures 18–21 (details may be found in [41] pp. 12–13).

In Figure 8, Figure 11, Figure 14, and Figure 17, the frequency characteristics determined for the *OPT* system with nonzero actuator power weights g_{23} (control *case III*) and different i_{max} values are presented. Figure 21 depicts time patterns obtained for zero and nonzero g_{23} values with the MR damper in passive mode ($i_{max} = 0$) and semi-active mode ($i_{max} = 1.0$ A) Due to lowering actuator power (Figure 17) (and so its mean force, see Figure 21), the maximum $A(x_1)$ values may be observed within the (3.3, 3.4)Hz neighbourhood (Figure 8), contrary to the configurations with $g_{23} = 0$ (Figures 6 and 7), for which $A(x_1)$ elevation may be observed at higher frequencies due to the more detrimental actuator response delay in the situation of its higher output force. However, for the (3.3, 3.4)Hz range, MR damper support was not beneficial (see Figures 8 and 21), as was discussed earlier (i.e., the MR damper semi-active operation resulted in a slightly smaller TVA stroke amplitude, while the actuator response delay was not that meaningful as for the higher frequencies). The influence of the actuator power weight on its operation is apparent in Figure 21—the actuator control signal $F_{a\ ctr}$ (and so its output force F_a) was clearly lowered for $g_{23} = 10^{10}$, and particularly for $g_{23} = 10^{11}$. This yielded significant actuator power reduction, i.e., below 0.19 W, regarding the control *case I* ($g_{23} = 0$), as shown in Figure 17 vs. Figures 15 and 16.

Three of the regarded control options deserve a special note: the *restricted force OPT* configuration, control *case I* ($F_{nom} = 6.25$ N, $i_{max} = 0.5$ A, $g_{23} = 0$) vs. the *restricted force GH* configuration ($F_{nom} = 6.25$ N, $i_{max} = 0.5$ A) vs. the *baseline* configuration, control *case III* ($F_{nom} = 12.5$ N, $i_{max} = 1.0$ A, $g_{23} = 10^{10}$). All three configurations yielded maximum x_1 deflection amplitudes of ca. 1.78 mm (Figures 7 and 8), which was more than a 30% reduction regarding the 0.0 A passive system (Figure 6), while the maximum TVA stroke amplitudes were close to those of the 0.0 A passive system. To obtain the primary structure deflection minimisation, both noted *restricted force OPT*/*GH* configurations required the MR damper of ca. 16 N maximum force and the actuator of 0.35 W nominal power, while the latter approach (*baseline* configuration, control *case III*) required the damper of 3.3 N maximum force and the actuator of 0.17 W nominal power, which is by far a preferable solution. Here comes forth the advantage of the properly tuned *OPT* solution (over the simple *GH* control with changeable F_{nom} and i_{max} values only) with its various optimisation fields (quality function components) to obtain a significantly better efficiency concerning the important aspect of the energy demand, associated with the g_{23} weight use, while the vibration attenuation efficiency was the same as for the *GH* configuration considered here.

Recapitulating, the control solutions that are particularly recommended are:

(1) *H-MR-TVA* system with *OPT* control *case I/GH baseline* configuration, characterised by the 57% maximum structure deflection reduction (regarding the passive configuration), ca. 0.76 W nominal actuator power, and ca. 32 N maximum MR damper force;
(2) *H-TVA* system with *OPT* control *case III baseline* configuration and $g_{23} = 10^{10}$, characterised by the 30% maximum structure deflection attenuation (regarding the passive configuration), 0.17 W nominal actuator power, and 3.3 N maximum (passive) damper force.

For higher actuator force solutions (as the former), the MR damper semi-active support with millisecond response time was greatly beneficial due to the substantial actuator response time delay related to the oscillation period at frequencies above 3.6 Hz (see Figures 5, 6 and 19). On the other hand, it may also be observed that the electric actuator cancelled the unwanted MR damper remanent force, as assumed previously—see Figures 17, 18, 19 and 20a,b,d.

Using a nonzero g_{221} value led to 40% MR damper force reduction ($F_{nom} = 12.5$ N, $i_{max} = 1.0$ see Figure 13); however, the cost was a 24% increased maximum structure deflection, and a 7.5% increased maximum actuator power, which rendered this solution aimless. The influence of the other weighting factors (g_{11}, g_{13}, g_{21}) was studied within the scope of the previous research [34,41]. The operation of the regarded system with MR damper control only (idling electric drive) was also studied before; in current research, it was regarded as aimless, as the already embedded electric actuator adds undesirable excess damping to the TVA system.

With the help of the dynamical similarity analysis that includes previously determined time and length scale factors ($s_T = 0.135$ and $s_L = 0.0176$, respectively) [53] in combination with force scale factor $s_F = 1.75 \cdot 10^{-3}$ [54], the results obtained in the current study may be used as the indicators of the demanded control forces (with regard to actual mass ratio) that have to be generated in the H-MR-TVA (H-TVA) system attached to the real-world Vensys82-class wind turbine structure. Full-scale implementation of the two exemplary control solutions (1) and (2) recommended above will require: (1) an actuator of 7.1 kN nominal force and 3.33 kW nominal power, plus an MR damper of 18.2 kN maximum force, (2) an actuator of 7.1 kN nominal force and 0.74 kW nominal power, plus a passive damper of 1.9 kN maximum force.

8. Conclusions

The purpose of this research was a real-time implementation and experimental study of the nonlinear optimal-based vibration control for a scaled wind turbine tower-nacelle model with the H-MR-TVA system, using the simultaneous operation of the small electric servo drive and the MR damper. With the use of commercially available hardware, the previously developed approach was successfully implemented and validated. The combined operation of the electric actuator and the MR damper in the H-MR-TVA *baseline* system led to a 35% maximum structure deflection reduction in relation to H-MR-TVA operation with MR damper in the passive mode (with zero current) and a 52% reduction compared to the previous research [41]. Both *GH* and *OPT* solutions guaranteed maximum deflection values close to 1.1 mm (the 57% reduction with regard to the best passive TVA configuration), using the MR damper of 32 N maximum force and actuator of 12.5 N nominal force and 0.76 W nominal power. This proved the effectiveness and validity of the adopted concept. No MR damper/actuator force tracking nor online vibration frequency determination were required, which decreased the control adequacy, especially during the multi-frequency and random vibration phases. The MR damper and actuator force constraints did not compromise the control quality. No offline calculation nor disturbance presumption were required for proper system operation.

An interesting alternative is the *OPT* system with the actuator power weight $g_{23} = 10^{10}$. It provided a 30% maximum structure deflection attenuation, regarding the passive configuration, while using a passive damper of 3.3 N maximum force and electric drive of

0.17 W nominal power, which was 22% of the *baseline* system nominal actuator power. This also makes evident the advantage of the properly tuned *OPT* solution (over the simple *GH* control) with its various optimisation fields, covered by the optimal control task quality index—it yielded significantly better energy efficiency marks compared to the *GH* approach exhibiting the same vibration attenuation properties. The *GH* control is devoted to the case when only the protected structure deflection has to be minimised, while the *OPT* concept coped well with different system constraints as, e.g., the TVA working space, the MR damper/actuator nonlinearities (including stroke and force limitations), the actuator power and energy demand, etc., which makes the proposed method a valuable real-time vibration control solution. However, the used electric drive response time is a substantial drawback of the regarded system; the actuator linear dynamics were not considered in this study, and this turned out to yield elevated vibration levels at higher frequencies (which may not be the case for other actuator types to be used, e.g., the electro-hydraulic one). Thus, the nearest research involves a (model) predictive optimal control with the actuator linear dynamics implemented to cope with this problem. Moreover, the possible increase in the sampling rate will benefit the *OPT* control.

Funding: This work was supported by AGH University of Science and Technology (research program no. 16.16.130.942).

Data Availability Statement: The data presented in this study are available on request.

Conflicts of Interest: The authors declare no conflict of interest.

References

1. Wang, X.; Gordaninejad, F. Lyapunov-Based Control of A Bridge Using Magneto-rheological Fluid Dampers. *J. Intell. Mater. Syst. Struct.* **2002**, *13*, 30–36. [CrossRef]
2. Weber, F.; Maślanka, M. Precise stiffness and damping emulation with MR dampers and its application to semi-active tuned mass dampers of Wolgograd Bridge. *Smart Mater. Struct.* **2014**, *23*, 015019.
3. Ali, S.F.; Ramaswamy, A. Hybrid Structural Control using magnetorheological dampers for base isolated structures. *Smart Mater. Struct.* **2009**, *18*, 055011. [CrossRef]
4. Esteki, K.; Bagchi, A.; Sedaghati, R. Semi-Active Tuned Mass Damper for Seismic Applications. In Proceedings of the Smart Materials, Structures & NDT in Aerospace, Montreal, Canada, 2–4 November 2011.
5. Kavyashree, B.G.; Patil, S.; Rao, V.S. Review on vibration control in tall buildings: From the perspective of devices and applications. *Int. J. Dynam. Control* **2020**, *9*, 1316–1331. [CrossRef]
6. Caterino, N. Semi-active control of a wind turbine via magnetorheological dampers. *J. Sound Vib.* **2015**, *345*, 1–17. [CrossRef]
7. Enevoldsen, I.; Mork, K.J. Effects of Vibration Mass Damper in a Wind Turbine Tower. *Mech. Struct. Mach.* **1996**, *24*, 155–187. [CrossRef]
8. Kirkegaard, P.H.; Nielsen, S.R.K.; Poulsen, B.L.; Andersen, J.R.; Pedersen, L.H.; Pedersen, B. Semiactive vibration control of a wind turbine tower using an MR damper. In *Structural Dynamics-EURODYN*; Grundmann, H., Schueller, G.I., Eds.; Swets & Zeitlinger: Lisse, The Netherlands, 2002.
9. Kucuk, I.; Yildirim, K.; Sadek, I.; Adali, S. Optimal control of a beam with Kelvin-Voigt damping subject to forced vibrations using a piezoelectric patch actuator. *J. Vib. Control* **2015**, *21*, 701–713. [CrossRef]
10. Xu, Z.D.; Zhu, J.T.; Wang, D.X. Analysis and Optimisation of Wind-Induced Vibration Control for High-Rise Chimney Structures. *Int. J. Acoust. Vib.* **2014**, *19*, 42–51. [CrossRef]
11. Bakhtiari-Nejad, F.; Meidan-Sharafi, M. Vibration Optimal Control of a Smart Plate with Input Voltage Constraint of Piezoelectric Actuators. *J. Vib. Control* **2004**, *10*, 1749–1774. [CrossRef]
12. Oates, W.S.; Smith, R.C. Nonlinear Optimal Control Techniques for Vibration Attenuation Using Magnetostrictive Actuators. *J. Intell. Mater. Syst. Struct.* **2008**, *19*, 193–209. [CrossRef]
13. Rotea, M.A.; Lackner, M.A.; Saheba, R. Active Structural Control of Offshore Wind turbines. In Proceedings of the 48th AIAA Aerospace Sciences Meeting Including the New Horizons Forum and Aerospace Exposition, Orlando, FL, USA, 4–7 January 2010.
14. Tsouroukdissian, A.; Carcangiu, C.E.; Pineda, A.I.; Martin, M. Wind Turbine Tower Load Reduction using Passive and Semiactive Dampers. In Proceedings of the European Wind Energy Association Annual Event, Brussels, Belgium, 14–17 March 2011.
15. Spencer, B.F., Jr.; Soong, T.T. New Applications and Development of Active, Semi-Active and Hybrid Control Techniques for Seismic and Non-Seismic Vibration in the USA. In Proceedings of the International Post-SMiRT Conference Seminar on Seismic Isolation, Passive Energy Dissipation and Active Control of Vibration of Structures, Cheju, Republic of Korea, 23–25 August 1999.
16. Zhang, Z.; Staino, A.; Basu, B.; Nielsen, S.R.K. Performance evaluation of full-scale tuned liquid dampers (TLDs) for vibration control of large wind turbines using real-time hybrid testing. *Eng. Struct.* **2016**, *126*, 417–431. [CrossRef]

17. Mensah, A.F.; Dueñas-Osorio, L. Improved reliability of wind turbine towers with tuned liquid column dampers (TLCDs). *Struct. Safety* **2014**, *47*, 78–86. [CrossRef]
18. Zhang, J.; Roschke, P.N. Active control of a tall structure excited by wind. *J. Wind. Eng. Ind. Aerodyn.* **1999**, *83*, 209–223. [CrossRef]
19. Den Hartog, J.P. *Mechanical Vibrations*; Dover Publications: Mineola, NY, USA, 1985.
20. Preumont, A.; Alaluf, D.; Bastaits, R. Hybrid Mass Damper: A Tutorial Example. In *Active and Passive Vibration Control of Structures*; Hagedorn, P., Spelsberg-Korspeter, G., Eds.; CISM International Centre for Mechanical Sciences; Springer: Vienna, Austria, 2014. [CrossRef]
21. Demetriou, D.; Nikitas, N. A Novel Hybrid Semi-Active Mass Damper Configuration for Structural Applications. *Appl. Sci.* **2016**, *6*, 397. [CrossRef]
22. Nakamura, Y.; Tanaka, K.; Nakayama, M.; Fujita, T. Hybrid mass dampers using two types of electric servomotors: AC servomotors and linear-induction servomotors. *Earthq. Eng. Struct. Dyn.* **2001**, *30*, 1719–1743. [CrossRef]
23. Nishimura, I.; Kobori, T.; Sakamoto, M.; Koshika, N.; Sasaki, K.; Ohrui, S. Active tuned mass damper. *Smart Mater. Struct.* **1992**, *1*, 306–311. [CrossRef]
24. Di Paolo, M.; Nuzzo, I.; Caterino, N.; Georgakis, C.T. A friction-based passive control technique to mitigate wind induced structural demand to wind turbines. *Eng. Struct.* **2021**, *232*, 111744. [CrossRef]
25. Shen, Y.J.; Wang, L.; Yang, S.P.; Gao, G.S. Nonlinear dynamical analysis and parameters optimization of four semi-active on-off dynamic vibration absorbers. *J. Vib. Control* **2013**, *19*, 143–160. [CrossRef]
26. Martynowicz, P. Vibration control of wind turbine tower-nacelle model with magnetorheological tuned vibration absorber. *J. Vib. Control* **2017**, *23*, 3468–3489. [CrossRef]
27. Martynowicz, P. Control of an MR Tuned Vibration Absorber for Wind Turbine Application Utilising the Refined Force Tracking Algorithm. *J. Low Freq. Noise Vib. Act. Control* **2017**, *36*, 339–353. [CrossRef]
28. Hu, Y.; He, E. Active structural control of a floating wind turbine with a stroke-limited hybrid mass damper. *J. Sound Vib.* **2017**, *410*, 447–472. [CrossRef]
29. Kim, H.T.; Kim, C.H.; Choi, S.B.; Moon, S.J.; Song, W.G. A novel triple actuating mechanism of an active air mount for vibration control of precision manufacturing machines: Experimental work. *Smart Mater. Struct.* **2014**, *23*, 077003. [CrossRef]
30. Han, C.; Choi, S.B.; Lee, Y.S.; Kim, H.T.; Kim, C.H. A new hybrid mount actuator consisting of air spring and magneto-rheological damper for vibration control of a heavy precision stage. *Sens. Actuator A Phys.* **2018**, *284*, 42–51. [CrossRef]
31. Brodersen, M.L.; Ou, G.; Høgsberg, J.; Dyke, S. Analysis of hybrid viscous damper by real time hybrid simulations. *Eng. Struct.* **2016**, *126*, 675–688. [CrossRef]
32. Hu, Y.; Chen, M.Z.Q.; Li, C. Active structural control for load mitigation of wind turbines via adaptive sliding-mode approach. *J. Frankl. Inst.* **2017**, *354*, 4311–4330. [CrossRef]
33. Fitzgerald, B.; Basu, B. Cable connected active tuned mass dampers for control of in-plane vibrations of wind turbine blades. *J. Sound Vib.* **2014**, *333*, 5980–6004. [CrossRef]
34. Martynowicz, P. Nonlinear Optimal-Based Vibration Control of a Wind Turbine Tower Using Hybrid vs. Magnetorheological Tuned Vibration Absorber. *Energies* **2021**, *14*, 5145. [CrossRef]
35. Koo, J.H.; Ahmadian, M. Qualitative Analysis of Magneto-Rheological Tuned Vibration Absorbers: Experimental Approach. *J. Intell. Mater. Syst. Struct.* **2007**, *18*, 1137–1142. [CrossRef]
36. Martynowicz, P. Study of vibration control using laboratory test rig of wind turbine's tower-nacelle system with MR damper based tuned vibration absorber. *Bull. Pol. Acad. Sci. Tech. Sci.* **2016**, *64*, 347–359.
37. Rosół, M.; Martynowicz, P. Implementation of LQG controller for wind turbine tower-nacelle model with MR tuned vibration absorber. *J. Theor. Appl. Mech.* **2016**, *54*, 1109–1123. [CrossRef]
38. Martynowicz, P.; Santos, M. Structural vibration control of NREL 5.0 MW FOWT using optimal-based MR tuned vibration absorber. In Proceedings of the 21st IFAC World Congress, Berlin, Germany, 11–17 July 2020.
39. Wang, L.; Liang, Z.; Cai, M.; Zhang, Y.; Yan, J. Adaptive Structural Control of Floating Wind Turbine with Application of MR Damper. *Energy Procedia* **2019**, *158*, 254–259. [CrossRef]
40. Martynowicz, P. Nonlinear optimal-based vibration control for systems with MR tuned vibration absorbers. *J. Low Freq. Noise Vib. Act. Control* **2019**, *38*, 1607–1628. [CrossRef]
41. Martynowicz, P. Real-time implementation of nonlinear optimal-based vibration control for a wind turbine model. *J. Low Freq. Noise Vib. Act. Control* **2019**, *38*, 1635–1650. [CrossRef]
42. Kciuk, S.; Martynowicz, P. Special application magnetorheological valve numerical and experimental analysis. *Control. Eng. Mater. Process. Diffus. Defect Data–Solid State Data Pt. B Solid State Phenom.* **2011**, *177*, 102–115. [CrossRef]
43. Laalej, H.; Lang, Z.Q.; Sapinski, B.; Martynowicz, P. MR damper based implementation of nonlinear damping for a pitch plane suspension system. *Smart Mater. Struct.* **2012**, *21*, 045006. [CrossRef]
44. Neelakantan, V.A.; Washington, G.N. Vibration Control of Structural Systems using MR dampers and a 'Modified' Sliding Mode Control Technique. *J. Intell. Mater. Syst. Struct.* **2008**, *19*. [CrossRef]
45. Lord RheoneticTM. *MR Controllable Friction Damper RD-1097-01 Product Bulletin*; Lord: Cary, NC, USA, 2002.
46. Bryson, A.E.; Ho, Y.C. *Applied Optimal Control*; Taylor & Francis: London, UK, 1975.
47. Itik, M. Optimal control of nonlinear systems with input constraints using linear time varying approximations. *Nonlinear Anal. Model. Control.* **2016**, *21*, 400–412. [CrossRef]

48. Shukla, P.; Ghodki, D.; Manjarekar, N.S.; Singru, P.M. A Study of H infinity and H2 synthesis for Active Vibration Control. *IFAC-PapersOnLine* **2016**, *49*, 623–628. [CrossRef]
49. Martynowicz, P.; Szydło, Z. Wind turbine's tower-nacelle model with magnetorheological tuned vibration absorber: The laboratory test rig. In Proceedings of the 14th International Carpathian Control Conference (ICCC), Rytro, Poland, 26–29 May 2013.
50. Martynowicz, P. Development of Laboratory Model of Wind Turbine's Tower-Nacelle System with Magnetorheological Tuned Vibration Absorber. *Solid State Phenom.* **2014**, *208*, 40–51. [CrossRef]
51. Martynowicz, P.; Rosół, M. Wind Turbine Tower-Nacelle System with MR Tuned Vibration Absorber: Modelling, Test Rig, and Identification. In Proceedings of the ICCC 2019: Proceedings of the 20th International Carpathian Control Conference, Kraków-Wieliczka, Poland, 26–29 May 2019.
52. Rosół, M.; Martynowicz, P. Identification of the Wind Turbine Model with MR Damper Based Tuned Vibration Absorber. In Proceedings of the ICCC 2019: Proceedings of the 20th International Carpathian Control Conference, Kraków-Wieliczka, Poland, 26–29 May 2019.
53. Snamina, J.; Martynowicz, P.; Łatas, W. Dynamic similarity of wind turbine's tower-nacelle system and its scaled model. *Solid State Phenom.* **2014**, *208*, 29–39. [CrossRef]
54. Snamina, J.; Martynowicz, P. Prediction of characteristics of wind turbine's tower-nacelle system from investigation of its scaled model. In Proceedings of the 6WCSCM: Sixth World Conference on Structural Control and Monitoring–proceedings of the 6th edition of the World conference of the International Association for Structural Control and Monitoring (IACSM), Barcelona, Spain, 15–17 July 2014.
55. Maślanka, M. Optimised semi-active tuned mass damper with acceleration and relative motion feedbacks. *Mech. Syst. Signal Process.* **2019**, *130*, 707–731. [CrossRef]
56. Ioffe, A.D.; Tihomirov, V.M. *Theory of Extremal Problems. Studies in Mathematics and its Applications*; North-Holland Publishing Company: Amsterdam, The Netherlands, 1979.
57. Pinto, S.G.; Rodriguez, S.P.; Torcal, J.I.M. On the numerical solution of stiff IVPs by Lobatto IIIA Runge-Kutta methods. *J. Comput. Appl. Math.* **1997**, *82*, 129–148. [CrossRef]
58. Festo Ltd. Festo Products. 2022. Available online: https://www.festo.com/gb/en/c/products-id_pim1 (accessed on 12 October 2022).
59. *TMS 60 Lbf Modal Shaker*; The Modal Shop Inc.: Cincinnati, OH, USA, 2010.
60. *InTeCo RT-DAC4/PCI Multi I/O Board. User's Manual*; InTeCo Ltd.: Krakow, Poland, 2002.
61. Sahu, G.N.; Singh, S.; Singh, A.; Law, M. Static and Dynamic Characterization and Control of a High-Performance Electro-Hydraulic Actuator. *Actuators* **2020**, *9*, 46. [CrossRef]